



**HAL**  
open science

## Nuclear Magnetic Resonance for interfaces in rechargeable batteries

Khashayar Bagheri, Michael Deschamps, Elodie Salager

► **To cite this version:**

Khashayar Bagheri, Michael Deschamps, Elodie Salager. Nuclear Magnetic Resonance for interfaces in rechargeable batteries. *Current Opinion in Colloid & Interface Science*, 2023, 10.1016/j.cocis.2022.101675 . hal-03925315

**HAL Id: hal-03925315**

**<https://hal.science/hal-03925315>**

Submitted on 5 Jan 2023

**HAL** is a multi-disciplinary open access archive for the deposit and dissemination of scientific research documents, whether they are published or not. The documents may come from teaching and research institutions in France or abroad, or from public or private research centers.

L'archive ouverte pluridisciplinaire **HAL**, est destinée au dépôt et à la diffusion de documents scientifiques de niveau recherche, publiés ou non, émanant des établissements d'enseignement et de recherche français ou étrangers, des laboratoires publics ou privés.

Copyright

# Nuclear Magnetic Resonance for interfaces in rechargeable batteries

Khashayar Bagheri,<sup>a,b</sup> Michael Deschamps<sup>a,b</sup> and Elodie Salager<sup>a,b,\*</sup>

<sup>a</sup> CNRS, CEMHTI UPR3079, Univ. Orléans, 1D avenue de la recherche scientifique, Orléans, France

<sup>b</sup> RS2E, CNRS FR3459, 15 rue Baudelocque, Amiens, France

[khashayar.bagheri@cnrs-orleans.fr](mailto:khashayar.bagheri@cnrs-orleans.fr)

[michael.deschamps@univ-orleans.fr](mailto:michael.deschamps@univ-orleans.fr)

[elodie.salager@cnrs-orleans.fr](mailto:elodie.salager@cnrs-orleans.fr)

\*corresponding author

## Abstract

Nuclear Magnetic Resonance (NMR) is a powerful technique to probe the local environment of atoms bearing a nuclear spin. Interfaces in a rechargeable battery, within multi-component electrode or electrolytes or between the electrodes and the electrolyte, are key to its function and lifetime. NMR spectroscopy of the solid phases in the battery participate in the understanding of the processes at these interfaces. The solid-state NMR community is still highly active for *ex situ* measurements. Dynamic Nuclear Polarization attracted interest thanks to its enhanced sensitivity. *In situ* spectroscopy and imaging prospered in the context of metallic Li or Na deposition, either as an ageing process in conventional Li or Na batteries, or as the primary process in a metal battery.

## Abbreviations

NMC<sub>xyz</sub>, nickel manganese cobalt lithium oxide  $\text{LiNi}_{0.x}\text{Mn}_{0.y}\text{Co}_{0.z}\text{O}_2$

EC, ethylene carbonate

DMC, dimethyl carbonate

FEC, fluoroethyl carbonate

PEO, poly(ethylene oxide)

LP30, commercial acronym for a solution of  $\text{LiPF}_6$  1 mol·L<sup>-1</sup> in EC:DMC (1:1 v:v)

DOL, 1,3 dioxolane

DME, dimethoxyethane

DFOB, difluoro(oxalato)borate anion

TFSI, bis(trifluoromethylsulfonyl)imide anion

FSI, bis(fluorosulfonyl)imide anion

SEI, solid electrolyte interface

CEI, solid electrolyte interface  
EXSY, Exchange Spectroscopy, NMR experiment  
DNP, Dynamic Nuclear Polarization  
MIDNP, Metal-Ion Dynamic Nuclear Polarization

## Introduction

Rechargeable batteries are complex and heterogeneous devices with numerous interfaces, which are essential as they are at the core of the battery function. The redox reactions used to store and release energy necessitate the (triple) contact of electrons, redox centres, and ions (commonly lithium) for charge balance. Side reactions also take place at interfaces and they are therefore of key importance for the battery lifetime.

Batteries are mainly composed of two electrodes, positive and negative, where the redox reactions take place (Figure 1). These are deposited on metallic foils acting as current collectors, usually copper for the negative electrode and aluminium for the positive electrode. The positive and negative electrodes are placed on each side of a separator that contains an electrolyte (ionic conductor but electrical insulator) for charge compensation during charge and discharge. The electrolyte can be a liquid soaking a porous material or a solid ionic conductor. In addition to the “macroscopic” interfaces - between current collector and electrode, electrode and electrolyte - other interfaces at the microscopic level can be of importance, especially inside the composite electrodes of the battery (active material and additives such as polymeric binders or electronic conductors, active material mixed with solid electrolyte in solid-state batteries...).

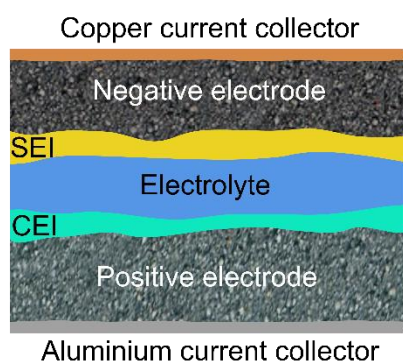


Figure 1. Schematics of a rechargeable battery. Interfaces appear between the current collectors and the electrodes, between the electrolyte and the negative electrode (solid electrolyte interface, or SEI) or with the positive electrode (cathode-electrolyte interface, or CEI) and within each composite component of the battery (electrode or electrolyte).

Nuclear Magnetic Resonance (NMR) is a powerful technique to probe the local environment of spin-bearing atoms. Recent reviews describe the considerable amount of work related to NMR studies on battery or battery-like devices [1,2]. Following the tradition of this journal, we focus on the reports that were published in the last three years and that shed new light on (side) reactions at interfaces. We will focus on the information gained from NMR spectroscopy and imaging on the solid phases in the battery, excluding specific diffusion and relaxation analyses of electrolytes. Further information on these applications can be found in recent reviews [3–5].

NMR is a bulk technique sensitive to the environment of the spin-bearing atom, so that the whole sample contributes to the signal. This is one of the great advantages of NMR, as the sample can be analysed without further preparation. Note the exception for electronic conductors such as bulk Li or Na, for which only a thin part on the surface (a few  $\mu\text{m}$ ) yields an NMR signal due to skin depth effects. Another asset of NMR is its atomic selectivity:  $^1\text{H}$ ,  $^{19}\text{F}$ ,  $^7\text{Li}$ ,  $^{31}\text{P}$ ,  $^{13}\text{C}$  and  $^{23}\text{Na}$  NMR spectra can be recorded independently and give information on the sample composition, dynamics and (sometimes) quantity.

Figure 2 summarizes the approaches that were used recently. Two main families of measurements, *ex situ* and *in situ*, can be performed to study the solid interphases in batteries. For *ex situ* NMR, the part of interest is extracted from the battery in an argon glovebox and transferred into the NMR sample holder. Magic-Angle Spinning (MAS) is a great tool to record resolved NMR spectra of solids and it is the main asset of *ex situ* NMR for the characterization of the solid components of a battery, especially for positive paramagnetic electrodes - electrodes containing transition metal ions with localised unpaired electrons such as  $\text{Co}^{2+}$ ,  $\text{Ni}^{2/3+}$ ,  $\text{Mn}^{4+}$ ,  $\text{Fe}^{2/3+}$ ... *Ex situ* NMR is traditionally performed to study the bulk changes in the solid parts for various states of charge of the battery [1,2], which is out of the scope of this contribution. More recently, it was applied to gain insight into the interface components of Li-ion batteries [6], especially the solid electrode-electrolyte interface (SEI) for the negative electrode [7–13], the solid electrolyte reactivity and dynamics [14,15] and the cathode-electrolyte interface (CEI) for the positive electrodes [16–18], but also for Na-ion batteries [19–22]. The liquid electrolyte stability (decomposition products on the surface) and the plating and stripping of metal (lithium, sodium) on negative electrodes were of particular interest.

The main issue for NMR studies of interphases is the small amount of material, so that the signals for the interphase are often hidden or negligible compared to the intense signals of the bulkier parts, such as the electrolyte or electrode. This is especially true for  $^7\text{Li}$  NMR from the active material or  $^1\text{H}$  NMR from the solvent in liquid electrolytes. Selective transfer from sensitive but less abundant atoms in the sample ( $^1\text{H}$ ,  $^{19}\text{F}$ ) was exploited to selectively enhance the signal from the solid electrode-electrolyte interface [10,14]. Specific NMR characteristics (shift, relaxation) were also used to be selective of the interface [7–9]. Introducing spatial selectivity is another way to study the interface. Selective enhancement by isotopic enrichment, especially with a  $^6\text{Li}$ -enriched lithium electrode - another NMR-active atom - is also one of the approaches to detect specifically mobile lithium atoms [14,15,18,23]. Dynamic Nuclear Polarization (DNP), can be performed to enhance the NMR signals but also to introduce an inherent spatial dependence: the magnetization enhancement takes place in the vicinity of the irradiated electrons and propagates throughout the sample [24–28]. Spatial selectivity can finally be obtained using Magnetic Resonance Imaging (MRI) techniques, so that signals from similar parts can be separated based on their location in the cell [29–36]. This is particularly useful when comparing the similar electrodes of a symmetrical Li//Li or Na//Na cell.

For *in situ* NMR, the full battery is placed within the NMR magnet and radiofrequency coil for the measurement (specific coils can be designed). Unfortunately, MAS NMR is not widely applicable to functional batteries due to the strong eddy currents generated by spinning metallic parts in a strong magnetic field, even though one promising attempt with limited electrochemical performance was published [37]. *In situ* NMR therefore suffers from lower resolution, so that *in situ* approaches concentrate on batteries with materials displaying strong variations in the NMR shifts upon charge-discharge, or in combination with *ex situ* studies

[23,32,33,36,38–50]. *In situ* NMR is advantageous as it is non-destructive - the battery does not need a destructive opening for the measurement - and it allows measuring the spectra for several states of charge on the *same* battery. In the *operando* mode (while current is flowing for the charge/discharge) it can detect transient phases in real time. This is of particular interest in batteries because of the strongly reducing environment, especially at the negative electrode on top of charge (near -3V versus the standard hydrogen electrode).

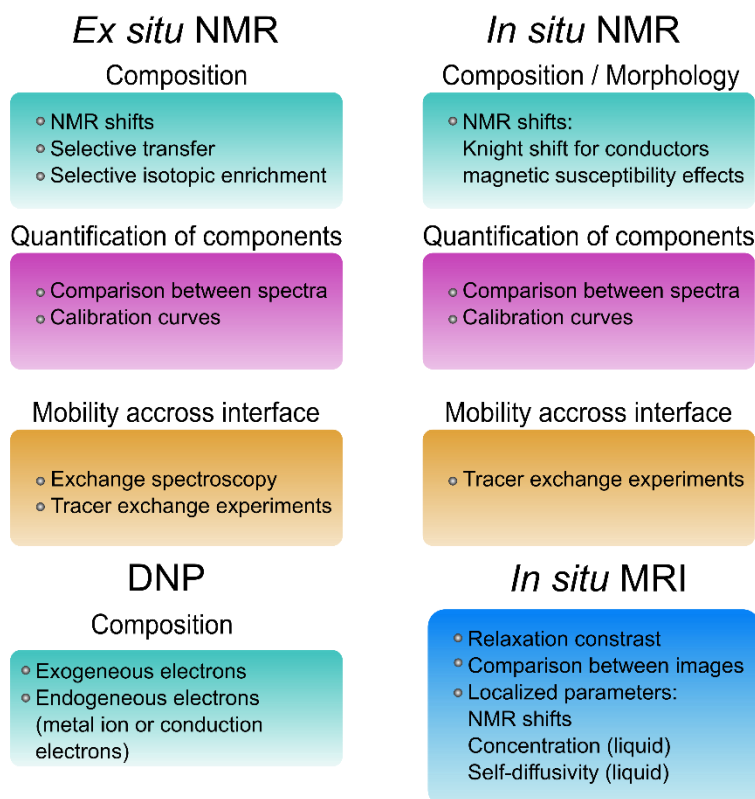


Figure 2. Approaches covered in this review that were used in recent years for the characterisation of interfaces in rechargeable batteries

## 1. *Ex situ* solid-state MAS NMR

This section focuses on the most recent studies of the solid compounds formed on the surface of the electrode (SEI and CEI) by *ex situ* solid-state NMR (SS-NMR). For older studies a nice review focusing on solid-state NMR of interfaces was published in 2018 by Haber et al [6]. A common approach to identify the components is to extract the SEI by dissolution in deuterated solvents ( $d_6$ -DMSO or  $D_2O$ ) and to record its  $^1H$ ,  $^{19}F$ ,  $^{13}C$  and  $^7Li$  liquid-state NMR spectra. A nice review was published in 2019 for such liquid-state NMR characterization [51].

Here most studies are performed using Magic Angle Spinning (MAS-NMR) to obtain higher resolution. Fast spinning of the sample around an axis oriented at the “magic-angle” ( $54.74^\circ$ ) with respect to the strong main magnetic field averages out the orientation-dependent

interactions that would otherwise broaden the spectrum. Fast spinning is required (15-60 kHz in rotors of 4 to 1.3 mm outer diameter) to achieve sufficient resolution.

Three directions for *ex situ* SS-NMR of battery interfaces have been pursued or explored: composition using NMR shifts, selective excitation or selective isotopic enrichment; quantification using a simple comparison of spectral areas or calibration curves; transport or mobility studies using Exchange Spectroscopy (EXSY) or tracer-exchange experiments (using  $^6\text{Li}$ -enriched metallic Li). Smart approaches using Dynamic Nuclear Polarization (DNP) were also developed to enhance sensitivity and selectivity to the interface and were combined with MAS-NMR. These studies will be mentioned in Section 2.

## 1.1. Interface between liquid electrolyte and negative electrode

The term “solid electrode-electrolyte interface (SEI)” is used to describe the phases formed at the interface between the negative electrode and the liquid electrolyte. The formation of the SEI is inevitable but the goal is to obtain a thin, stable and insulating film that prevents further reduction of the electrolyte. The most common electrolyte for Li-ion batteries was successfully designed for graphite electrodes and is commercially established. It is a solution of lithium hexafluorophosphate ( $\text{LiPF}_6$ ) in a mixture of alkyl carbonates - typically ethylene carbonate (EC) and dimethyl carbonate (DMC). The SEI is assumed to be composed of organic and inorganic products of decomposition formed by the reaction of the electrode with the electrolytic salt but also the alkyl carbonate solvents. The interface between the graphite electrode and the electrolyte is well-controlled and relatively well-characterised so that most recent NMR studies concentrate on the SEI for other materials.

### 1.1.1. Silicon and silicon-graphite blends

Among newer negative electrodes, silicon is expected to expand the volume capacity of Li-ion battery cells for electrified automotive applications. One of the issues with silicon is the huge volume expansion obtained at full capacity ( $\text{Li}_{15}\text{Si}_4$ ) that provokes delamination from the current collector or cracking of the electrode by pulverisation, followed by the formation of an additional SEI and an increase in the capacity loss. Recent NMR studies focus on the effect of additional salts in the electrolyte on the composition of the SEI of silicon electrodes, using one-dimensional NMR spectra of  $^{19}\text{F}$ ,  $^7\text{Li}$ , and  $^{29}\text{Si}$ .

A first study reports on the addition of magnesium-bis(trifluoromethylsulfonyl)imide  $\text{Mg}(\text{TFSI})_2$  to the liquid electrolyte for silicon electrodes [7].  $^7\text{Li}$  and  $^{29}\text{Si}$  MAS-NMR indicated that the reactivity of ethylene carbonate in the electrolyte with model lithium-magnesium silicides was hindered compared with model lithium silicides. The shifts in the  $^7\text{Li}$  and  $^{29}\text{Si}$  NMR spectra of lithiated silicon electrodes (11.1 ppm and -55 ppm compared to 6.7 ppm and -127 ppm for  $\text{Li}_{15+x}\text{Si}_4$ ) indicated  $\text{Mg}^{2+}$  doping upon first lithiation, in agreement with other techniques. The authors suggest that this doping happens on the surface of silicon and enhances its stability versus alkyl carbonates.

Other studies concentrate on the SEI composition using *ex situ*  $^7\text{Li}$  and  $^{19}\text{F}$  MAS-NMR on delithiated silicon electrodes. Using calibration curves, the amount and partial nature of

lithiated species in the SEI were quantified for pure silicon cycled with superconcentrated lithium bis(fluorosulfonyl)imide (FSI) in ionic liquid electrolyte [8]\* and silicon-graphite blends cycled in an alkyl carbonate electrolyte, LiPF<sub>6</sub> in dimethyl carbonate : fluoroethyl carbonate (DMC:FEC, 70:30) [9].

The specific shift of LiF (-204 ppm) in <sup>19</sup>F spectra enables its quantification, which was then used to interpret the <sup>7</sup>Li spectra in terms of LiF content and “other lithiated components”. The exact nature of the latter could not be identified and it was quantified as a single component. The presence of lithiated compounds different from LiF seemed correlated with a better electrochemical performance in the case of superconcentrated ionic liquid electrolytes [8]\*.

### 1.1.2. Metallic Li

Lithium-metal batteries are another subject of active research. Metallic lithium would be a perfect negative electrode with superior capacity, but it is plagued by inhomogeneous deposition often called “filaments” or “dendrites”. These enhance the lithium surface area and the electrolyte decomposition and SEI formation are increased on these newly exposed surfaces. MAS-NMR provides information on the nature of the SEI, on mobility across the interface and it also offers (semi) quantitative information on amounts and relative composition.

An additional challenge here is the electrical conductivity of the metal. Spinning of conductors in a strong magnetic field is usually an issue due to strong induced eddy currents that lead to braking and heating. This is avoided by cutting the conductor into small pieces and diluting it in a non-reactive dried powder (usually dried KBr), or by scraping the surface to retrieve the SEI, trying not to take metal off (at the expense of quantitativity).

*Ex situ* quantification of the <sup>7</sup>Li-containing compounds in the SEI of metallic Li was performed by May et al. [10] for multiple charge-discharge cycles of a symmetric Li//Li cell in a bi-salt electrolyte in etherated solvents (0.5 M LiNO<sub>3</sub> and 0.5 M LiTFSI solutions in 1,3 dioxolane: dimethoxyethane (DOL:DME, 1:1, v/v) ). The lack of resolution in the <sup>7</sup>Li MAS-NMR spectrum of the SEI was compensated by selective excitation of <sup>7</sup>Li near <sup>1</sup>H and <sup>7</sup>Li near <sup>19</sup>F (using <sup>1</sup>H→<sup>7</sup>Li and <sup>19</sup>F→<sup>7</sup>Li cross-polarization) to analyse the SEI only. These selective spectra then helped constraining the fitting model of the total spectrum with three components: Li near F, Li near H and “other” (mostly Li<sub>2</sub>O natively found on the metal surface). Addition of 0.5 M LiNO<sub>3</sub> and 0.5 M LiTFSI to DOL:DME resulted in higher coulombic efficiencies and smoother deposits. MAS-NMR detected a more heterogeneous SEI (additional protonated decomposition products) and thicker (or denser) SEI compared to 1 M LiTFSI in DOL: DME and it was concluded that the LiNO<sub>3</sub> additive did not result in thinner or more homogeneous SEI.

The better electrochemical performance was rather assigned to better transport properties of lithium across the resulting SEI, based on <sup>7</sup>Li-<sup>7</sup>Li exchange spectroscopy (EXSY) experiments. These measurements are able to probe spin diffusion and/or dynamics between NMR-resolved Li sites at equilibrium in the millisecond to second timescale (Figure 3a,b). Spin diffusion was excluded here by the increasing intensity of the cross-peaks at higher temperature. Spontaneous lithium exchange was instead confirmed across the interface between metallic Li and the SEI (at equilibrium).

EXSY experiments are extremely complementary to fast and local diffusion measurements (e.g. NMR relaxation). Ionic transport may indeed be fast in a limited zone and microsecond timescale, but limited for longer distances when grain boundaries or interfaces are present. EXSY probes dynamics specifically between NMR-resolved sites and it is therefore specific of an interface. One should also be aware that the information is averaged over a longer timescale (millisecond to second) and that in this case it gives insight into the exchange currents across the interface. The  $^7\text{Li}$  exchange rates, between Li metal and Li in the various components of the SEI, were here determined by fitting the evolution of 1D EXSY experiments with increasing mixing times (Figure 3c). These  $^7\text{Li}$  exchange rates increased from 5 to 80  $\text{s}^{-1}$  with the  $\text{LiNO}_3$  additive, indicating an improvement of general mobility. As the SEI was neither more homogeneous nor thinner, the decomposition products of the nitrate ions ( $\text{Li}_x\text{N}_y\text{O}_z$ ) onto  $\text{Li}_2\text{O}$  were hypothesized to facilitate contact and transport in the SEI.

The smooth deposits of metallic Li obtained with the addition of alkali  $\text{K}^+$  ions into the electrolyte were also studied using a combination of *ex situ* solution NMR in the electrolyte (extracted from the separator by  $\text{d}_6$ -DMSO) and *ex situ* MAS-NMR of the insoluble species on the surface of the electrode [11].  $\text{KPF}_6$  was added to a standard electrolyte ( $\text{LiPF}_6$  in EC:DMC) and symmetric Li//Li cells were charged and discharged. The insoluble species present on the Li microstructures were scraped off by a razor blade and mixed with KBr for MAS-NMR studies. Quantification of  $^1\text{H} \rightarrow ^{13}\text{C}$  cross-polarization measurements showed a decrease in SEI of around 20%. Direct  $^{13}\text{C}$  excitation spectra of cells cycled in  $^{13}\text{C}$ -enriched electrolyte identified a reduced decomposition of the solvent into  $\text{Li}_2\text{CO}_3$  (169 ppm) and poly-ethylene-oxide-type fragments (68 ppm) and an increased proportion of polycarbonate moieties (161 ppm) at the Li-electrolyte interface. This change in composition probably takes part in the smoother Li plating.

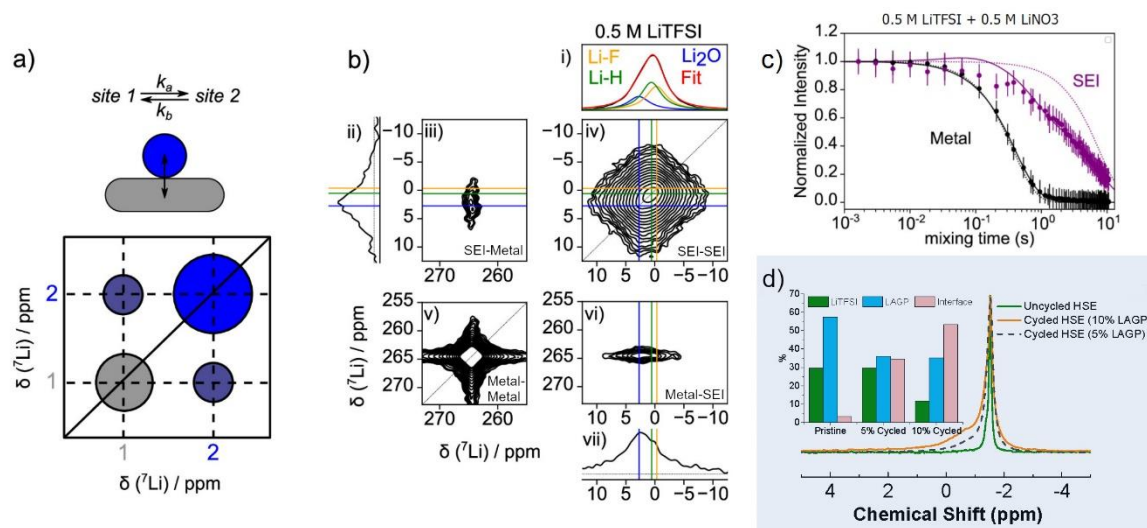


Figure 3. EXSY and tracer-exchange experiments (a) 2D  $^7\text{Li}$ - $^7\text{Li}$  EXSY cartoon showing chemical exchange between the SEI (blue) and Li metal (gray), with crosspeaks shown in grayish-blue. (b) Representative 2D solid-state  $^7\text{Li}$ - $^7\text{Li}$  NMR EXSY contour plots and corresponding 1D slices for electrolyte decomposition products deposited on the surface of Li metal after cycling in 0.5 M LiTFSI electrolyte. The sample was dried prior to analysis. The separate panels denote (i) 1D row slices at the LiF chemical shift in the indirect dimension ( $-0.33$  ppm), (ii) 1D column projections at the Li metal chemical shift in the direct dimension (264.5 ppm), (iii-vi) contour plots zoomed in to show SEI  $\rightarrow$  metal exchange, SEI  $\leftrightarrow$  SEI

exchange, metal  $\leftrightarrow$  metal exchange, and metal  $\rightarrow$  SEI exchange, respectively, and (vii) 1D row slices at the Li metal chemical shift in the indirect dimension. (c) 1D  $^7\text{Li}$  MAS EXSY raw data (circles) and Bloch–McConnell fits (solid lines) for Li metal (black) and the SEI (purple) formed upon cycling Li metal anodes in 0.5 M LiTFSI + 0.5 M  $\text{LiNO}_3$  electrolyte. Intensities normalized to the first data point are shown as a function of mixing time. Disagreement between the data (circles) and the expected  $T_1$  decay (dotted line) shows that chemical exchange occurs in the sample. (d)  $^6\text{Li}$  NMR spectra and (inset) contribution of each peak used for the fitting: LiTFSI, LAGP and new lithiated environment) of the hybrid solid electrolyte 10% LAGP/ 90% PEO-succinonitrile-LiTFSI, before and after cycling. A new environment centered at -0.75 ppm appears in the electrolyte after polarization between two  $^6\text{Li}$ -enriched Li foils and its area (pink in inset) changes with the LAGP content (10% or 5%), so it was assigned to the interface between LAGP and the polymer matrix. The proportion of the  $^6\text{Li}$  signals for LAGP (blue in inset) and for the interface (pink in inset) are enhanced upon cycling and indicate that the conduction pathways of Li ions are located in both the LAGP component and the LAGP-polymer interface. (a-c) Adapted with permission from [10]. Copyright 2021 American Chemical Society and (b) copied from [14]\*\* (CC BY-NC-ND licence).

### 1.1.3. Anode-free cells

Anode-free cells for lithium-metal batteries were first proposed in 2000, but they have been really attracting much interest as a way to obtain a thinner and more homogeneous metallic lithium negative electrode in the last three years. The metallic Li negative electrode is generated *in situ* during the first charge through plating on a copper current collector.

Zheng et al. studied the positive effect of two additives, vinylene carbonate (VC) and lithium difluorophosphate (LiDFP) in alkyl carbonate-based electrolytes with Li//Cu cells [12]. Additional LiF,  $\text{Li}_3\text{PO}_4$  and P–O–C species were observed in the SEI by  $^6\text{Li}$  (better resolution compared to  $^7\text{Li}$ ),  $^{31}\text{P}$  and  $^{19}\text{F}$  MAS-NMR compared to the standard electrolyte, while the amount of  $\text{Li}_2\text{CO}_3$  was lower. The former species, beneficial for the ionic conductivity of the SEI, were assumed to arise from LiDFP decomposition, a mechanism that would prevent  $\text{Li}_2\text{CO}_3$  formation. VC was found to limit the amount of LiDFP decomposition and to ensure the formation of a thin SEI.

The morphology of plated Li is strongly influenced by the surface chemistry of the Cu current collector and MAS-NMR was one of the techniques used to characterize and quantify the SEI. Copper oxide, superoxide and hydroxide are naturally present on the surface, which may be electrochemically active or influence the electrochemical Li plating. Menkin et al. studied the effect of this native interphase layer (N-SEI) on the plating process [13]. N-SEI was compared with electrochemically-generated SEI (e-SEI) by  $^7\text{Li}$  and  $^{19}\text{F}$  NMR. The N-SEI was generated by immersion of pre-treated (with acid) Cu in a  $\text{LiPF}_6$ -based electrolyte. The e-SEI was then generated on Cu using a voltage hold at 2 V in a Li//Cu cell with the same electrolyte. In both SEI,  $\text{LiPF}_6$  salts (-72 and -85 ppm) and their decomposition products  $\text{LiPO}_x\text{F}_y$  (-202 and -204 ppm) as well as LiF (-204 ppm) were detected with  $^{19}\text{F}$  MAS-NMR, while a peak assigned to fluorides near Cu (-225 ppm) only appeared in the N-SEI. The  $^7\text{Li}$  spectra are not well resolved, but the broader  $^7\text{Li}$  spectrum of e-SEI was assigned to a more heterogeneous composition. The efficiency of the Li plating–stripping process and the morphology of the plated Li were further characterised by *in situ* NMR (see section 3.1).

## 1.2. Interface between solid electrolyte and electrode

Solid electrolytes are intensely studied as they could advantageously replace the liquid flammable alkyl carbonate solvents. Solid electrolytes act as conductors of lithium or sodium cations and can be sorted into two main families, inorganic (sulfides, oxides, phosphates) and organic (polymers). Their implementation has been hindered so far due to low conductivity at room temperature and/or high reactivity with the electrodes. Recently, hybrid solid electrolytes mixing several types have been proposed to combine the best of both worlds.

Wagemaker *et al.* summarised their results in a recent review [14]\*\*. Exchange experiments (EXSY) were used to study dynamics at the grain boundaries between components in hybrid electrolytes and between electrolyte and electrode, by mixing them in the powder form. EXSY experiments can be performed as 1D or 2D, using either  $^7\text{Li}$  or  $^6\text{Li}$  NMR, and they probe spin diffusion and the dynamics of Li between NMR-resolved Li sites in a sample at equilibrium (aka on average the structure and composition do not change). As  $^6\text{Li}$  is not abundant, no spin diffusion is expected, and the results indicate directly Li dynamics. Exchange rates in the range  $1\text{-}100\text{ s}^{-1}$  can be probed using this technique; the activation energy for the corresponding processes can be extracted from rates measured at several temperatures. In these studies, the exchange MAS-NMR spectra measured on a mixture of sulfide electrolytes ( $\text{Li}_6\text{PS}_5\text{Cl}$  and  $\text{Li}_6\text{PS}_5\text{Br}$ ) indicated that dynamics across the boundary was not the limiting step. Dynamics at the electrolyte-electrode interface ( $\text{Li}_6\text{PS}_5\text{Cl}_{0.5}\text{Br}_{0.5}$  or  $\text{Li}_7\text{P}_3\text{S}_{11}$  with  $\text{Li}_2\text{S}$ ,  $\text{Li}_{1+x}\text{Al}_x\text{Ge}_{2-x}(\text{PO}_4)_3$  with  $\text{LiV}_2\text{O}_5$ ) was further explored to demonstrate that the Li dynamics across the interface was drastically lowered upon cycling. For sulfides it was assigned to the decomposition of the electrolyte into poorly conductive compounds at the interface, while for oxides a space-charge layer (arising from differences in chemical potential) was deemed responsible for the lowered dynamics across the interface. A  $\text{LiI}$  coating (designed to alleviate decomposition) was characterised using this technique. Its mixture with the  $\text{Li}_6\text{PS}_5\text{Cl}$  electrolyte and  $\text{Li}_2\text{S}$  electrode displayed Li exchange across the interface similar to that of the electrolyte-electrode mixture, indicating that this coating did not hinder transport for solid-state battery assemblies.

Wagemaker *et al.* also probed the exchanges through the interface, driven by the applied current, using the tracer-exchange approach to identify the main conduction pathways in sulfide electrolytes and hybrid solid electrolytes [14]\*\*, based on the technique popularized by Hu *et al.* [15]. Tracer-exchange NMR takes advantage of the two isotopes of lithium to follow their diffusion pathways between materials.  $^6\text{Li}$  and  $^7\text{Li}$  NMR spectra can be recorded independently thanks to their separated Larmor resonance frequencies (58.9 and 155.5 MHz for a 9.4 T, respectively).  $^6\text{Li}$ -enriched metallic foils were used as positive and negative electrodes and assembled with the natural abundance (93%  $^7\text{Li}$ ) solid electrolyte under study, polymeric (PEO-succinonitrile-LiTFSI) and inorganic (LAGP). Successive cycles of polarization resulted in selective  $^6\text{Li}$ -enrichment of the Li sites in the solid electrolyte that are active in Li transport. In Figure 3d the  $^6\text{Li}$  NMR spectra indicate that the ionic conduction pathways in the hybrid electrolyte are located in the LAGP component and in a new environment assigned to the LAGP-polymer interface.

Further spatial selectivity of the interface can be obtained in hybrid solid electrolytes, using an approach similar to that described for the liquid electrolyte-electrode interface (section 1.1). The lithiated interphase inside the hybrid solid electrolyte, between the organic ( $^1\text{H}$ ,  $^{19}\text{F}$ ,  $^6\text{Li}$ ) and inorganic ( $^{31}\text{P}$ ,  $^6\text{Li}$ ) parts, is selectively excited through  $^1\text{H}\rightarrow^6\text{Li}$ ,  $^{19}\text{F}\rightarrow^6\text{Li}$  and  $^{31}\text{P}\rightarrow^6\text{Li}$  NMR transfers (cross-polarization) to identify the contributions of the organic and inorganic components. Combined with tracer-exchange NMR, the  $^6\text{Li}$  spectra obtained by  $^1\text{H}\rightarrow^6\text{Li}$  cross-polarization transfers are selective of the interface and the ions involved in Li transport. This approach demonstrated that the interface between  $\text{Li}_{1.5}\text{Al}_{0.5}\text{Ge}_{1.5}(\text{PO}_4)_3$  (LAGP) and the polymer matrix (poly-ethylene-oxide, PEO) was the main path for diffusion in that hybrid solid electrolyte [14]\*.

### 1.3. Interface between liquid electrolyte and positive electrode

Although the interest is more recent, the cathode-electrolyte interface (CEI) is also of importance for cathode materials. *Ex situ* studies of the interface between the liquid electrolyte and the positive electrode suffer from low sensitivity and low resolution due to the paramagnetism of most positive electrodes, so that only a few NMR studies were reported recently. Paramagnetism arises from partially localized unpaired electrons on the transition metal centers; interactions between the electronic spin and the nuclear spin result in broadened and shifted NMR peaks, making the detection and characterization challenging. In 2019 Bichon et al. investigated the effect of aqueous processing on the surface composition and performance of  $\text{LiNi}_{0.5}\text{Mn}_{0.3}\text{Co}_{0.2}\text{O}_2$  (NMC532) electrodes. The surface chemistry of NMCs after exposure to air and moisture is well-studied; less after water immersion. Aqueous processing is an approach explored to replace the toxic *N*-methyl-2-pyrrolidone (NMP) solvent used in standard deposition of the electrodes as a slurry on the current collector. The surface of the NMC electrode after immersion in water and evaporation was characterised using single pulse  $^7\text{Li}$  MAS NMR and its Li content was quantified using calibration curves [16]. Acidification of the aqueous solution with  $\text{H}_3\text{PO}_4$  (1 wt % NMC) was performed to mitigate corrosion of the aluminium current collector and compared to natural-pH solution. The addition of  $\text{H}_3\text{PO}_4$  resulted in an increased amount of Li-containing compounds on the surface of the NMC532 particles, assigned to Li-transition metal phosphates, in addition to the usual hydroxides and carbonates. This additional depletion of Li from the electrode impacted the initial capacity but provided long-term cycling comparable to the standard NMP-processing protocol.

The composition of the CEI on a  $\text{LiNi}_{0.8}\text{Mn}_{0.1}\text{Co}_{0.1}\text{O}_2$  (NMC811)//Li cell cycled with standard LP30 electrolyte, a solution of  $\text{LiPF}_6$   $1\text{ mol}\cdot\text{L}^{-1}$  in EC:DMC (1:1 v:v), could be determined at full charge [17]. The lower paramagnetism of the NMC811 electrode at full lithiation creates a reasonable broadening and longitudinal relaxation of the  $^{13}\text{C}$  signal of the spectrum of the CEI, so that it can be acquired with good resolution using direct excitation. Lithium carbonate and carboxy moieties ( $\text{RCO}_2\text{Li}/\text{H}$ ) were observed in close proximity with the NMC811 surface (<1 nm based on EPR measurements of electron-carbon coupling and a specific spinning sideband manifold). Other  $^{13}\text{C}$  signals were assigned to decomposition products (from the alkyl carbonates) deposited further from the NMC811 grains, such as saturated and unsaturated alkyl chains and poly-ethylene-oxide (PEO) chains. Based on other techniques such as X-ray photoemission electron microscopy (XPEEM), the authors showed that  $\text{LiF}$  was also

preferentially deposited on the surface of NMC grains - but it could not be detected by  $^{19}\text{F}$  MAS-NMR. This lack of signal was assigned to a strong coupling with the paramagnetic centers in NMC811 that would broaden it beyond detection. The susceptibility discontinuity at the surface of the NMC811 particles may also be a non-negligible source of broadening.

Finally, the influence of an alkylated silicate coating on the dynamical exchange at the interface between the liquid electrolyte and a Li and Mn-rich  $\text{LiNi}_x\text{Mn}_y\text{Co}_z\text{O}_2$  (LMR-NMC) electrode was studied by Haber et al. using specific  $^6\text{Li}$ -enrichment [18]\*\* for spatial selectivity.  $^6\text{Li}$ -enriched LMR-NMC electrodes were soaked in a natural abundance solution of  $\text{LiPF}_6$  in alkyl carbonate (electrolyte) and the amount of  $^6\text{Li}$  in the electrode extracted from the electrolyte was monitored by  $^6\text{Li}$  MAS-NMR. While the uncoated electrode maintained its  $^6\text{Li}$  enrichment, the coated electrode lost  $^6\text{Li}$  progressively due to an increased exchange with the electrolyte, which demonstrated increased dynamics across the interface. That is assumed to be beneficial for the rate capacity of the electrode.

## 1.4. Metallic Na - liquid electrolyte interface

Na-ion batteries have fostered interest due to the higher availability of Na in the environment. As for Li-ion batteries, MAS-NMR - in combination with other techniques – is a powerful tool to investigate structural changes in the electrodes and solid electrolytes [1,2].

The analysis of the solid-electrolyte interface for metallic Na by *ex situ* MAS-NMR was only performed - to the best of our knowledge - for negative electrodes with well-separated  $^{23}\text{Na}$  NMR shifts and diluted for counteracting their electrical conductivity, or for an interphase scraped mechanically from the electrode.

The composition of the SEI on the surface of metallic Na electrodeposited on Cu (after multiple charge-discharge cycles, in Na//Cu cells) was characterised by *ex situ*  $^{23}\text{Na}$  MAS-NMR, and compared for propylene-carbonate-based electrolytes, with and without the fluoroethylene carbonate (FEC) additive [29]. NaF and NaH were identified in the FEC-containing electrolyte, based on their typical  $^{23}\text{Na}$  shift (7.2 and 18.8 ppm, respectively). NaH only appeared in the standard electrolyte. The remaining broad components were separated into “organic” and “inorganic” components based on spectral edition using  $^1\text{H} \rightarrow ^{23}\text{Na}$  cross-polarization transfer. This information was used to fit quantitative 1D  $^{23}\text{Na}$  MAS-NMR spectra, in which the proportion of the organic part was shown to be reduced drastically upon the addition of FEC. This effect was assigned to a lower amount of solvent decomposition replaced by FEC decomposition upon cycling. The improved long-term behaviour was assumed to arise from a better ionic conductivity of the inorganic-rich SEI.

The SEI obtained in symmetric Na//Na cells for a sodium difluoro(oxalato)borate (NaDFOB) salt in alkyl carbonate electrolytes was also analysed and compared to that obtained with the standard  $\text{LiPF}_6$  electrolytic salt [19]. DFOB was shown by *ex situ*  $^{23}\text{Na}$  and  $^{11}\text{B}$  MAS-NMR to decompose sacrificially and prevent the decomposition of the alkyl carbonate solvents. Fits were performed based on previous assignments for tetrafluoroborate, oligomeric borates, sodium oxalate and carbonate. The SEI composition was deemed stable from the 50<sup>th</sup> cycle based on almost unchanged  $^{23}\text{Na}$  and  $^{11}\text{B}$  NMR spectra for 100 and 200 cycles.

More recently, the SEI formed on Na electrodes cycled in superconcentrated NaFSI (3.8 M) in ionic liquids has been investigated by MAS-NMR, in the case of mesoporous carbon [20] and metallic Na [21,22]. *Ex situ*  $^{23}\text{Na}$  and  $^{19}\text{F}$  MAS-NMR were used to characterise the SEI contents and identified large amounts of NaF formed on the mesoporous carbon. The good cycling properties in the superconcentrated ionic liquid were thus attributed to a highly ionic conductive inorganic SEI. For Na electrodes, a small amount of water (1000-5000 ppm) was shown to be an interesting additive for ionic liquid electrolytes in Na-ion batteries. NaF,  $\text{Na}_2\text{O}$  and a Na-FSI complex were detected within the SEI. The  $\text{Na}_2\text{O}$  content decreased and the Na-FSI complex increased for the batteries with water additive. Water was assumed to facilitate the formation of Na-FSI. $\cdot\text{xH}_2\text{O}$  complexes, which would result in a more homogeneous SEI deposit on the electrode and better long-term cycling.

## 1.5. Accessing information directly from oxygen

$^{17}\text{O}$  MAS-NMR is also an interesting probe for characterising the bulk electrode or the electrode-electrolyte interface. Its poor sensitivity, due to the very low abundance of the NMR-active isotope (0.04%) combined with broadening from its quadrupolar nature, is however a difficulty.  $^{17}\text{O}$  enrichment is usually necessary and is expensive. Recently, Laurencin et al. introduced a mechanochemistry-mediated isotopic labelling that only requires a few drops of  $^{17}\text{O}$ -labelled water [52]. This approach was extended to  $\text{Li}_2\text{MnO}_3$ ,  $\text{Li}_2\text{RuO}_3$  and  $\text{LiCoO}_2$  by Geng et al. [53].  $^{17}\text{O}$  signal loss upon lithiation was assigned to a strong electronic delocalisation from paramagnetic Co onto the  $\text{CoO}_2$  layer. This approach is however most promising for MAS-NMR studies of non-paramagnetic  $^{17}\text{O}$  environments in battery materials.

## 2. DNP

Dynamic Nuclear Polarization (DNP) has triggered enthusiasm in the NMR community because it can enhance sensitivity in solid-state NMR. Here we will review recent applications; nice recent reviews by Leskes et al. [24,25] cover DNP studies for solids and batteries in full detail. In DNP, a large electronic spin polarisation is transferred onto the nuclear spins of interest using a microwave source. There are two main DNP approaches for solids. If the material does not contain suitable unpaired electrons, exogenous DNP is applied: the material is impregnated by a solution containing a specific radical. When possible, endogenous DNP is performed using the electrons in transition metal ions (Metal-Ion Dynamic Nuclear Polarization, MIDNP) or conduction electrons. The experiments usually need to be performed at low temperature with magic angle spinning, with the notable exception of metallic lithium. It is important to note that DNP was only performed *ex situ* as it usually requires low temperature to lower electronic relaxation (with the notable exception of metallic Li).

### 2.1. Cathode-electrolyte interface

Exogenous DNP brings two advantages to NMR of the liquid-solid interface: it brings additional sensitivity and spatial selectivity for the interphase. In that case, hyperpolarization is indeed transferred from the soaking solution to the closest atoms, aka those in the CEI.

Hestenes et al. reported exogeneous DNP MAS-NMR to study the cathode-electrolyte interphase in  $\text{Li}_2\text{RuO}_3$  (a model for Li-excess cathodes) charged-discharged in classical LP30 [26]. Thanks to the transfer of polarization from  $^1\text{H}$  in the radical solution to  $^{13}\text{C}$  in the interphase, the CEI composition was determined as a combination of alkyl- and polycarbonates, poly (ethylene oxide), lithium acetate, fluoride and carbonate and acetals. Quantification is imprecise with DNP, but regular  $^{13}\text{C}$  CPMAS NMR was used to semi-quantify the variations upon cycling by comparison with the  $^{13}\text{C}$  peak of PVDF in the electrode. The paper demonstrated that the composition of the CEI evolved upon charge, leading to a PEO-only CEI at full charge. This supports the hypothesis of cross-talk between the interphases at the cathode (CEI) and at the anode (SEI).

In another work, Leskes and collaborators analyzed the structure of an artificial CEI created by atomic layer deposition of alkylated  $\text{Li}_x\text{Si}_y\text{O}_z$  [18\*\*,27]. A specific coating was applied to Li-ion excess cathode to act as an artificial CEI and prevent the formation of the detrimental “native” CEI. Exogenous DNP combined with selective transfer from  $^1\text{H}$  to  $^7\text{Li}$  or  $^{29}\text{Si}$  atoms provided the “outer” picture of the coating layer and indicated that the Li and Si atoms were in separated phases, with Li atoms distributed throughout the CEI [27]. The coating was suggested to be a thin layer of amorphous silicon terminated with siloxanes or alkylated Si. Haber et al. studied further this type of coating by measuring both the “inner” (Figure 3a) and the “outer” (Figure 3b) sides of the CEI on  $\text{Fe}^{3+}$ -doped model  $\text{TiO}_2$  with exogeneous DNP and metal-ion DNP [18]\*\*. MIDNP is complementary to exogenous DNP, as it can be performed using a paramagnetic dopant inside the electrode ( $\text{Fe}^{3+}$  here) as the source of hyperpolarization. The authors detected Si in less alkylated silicon environments in the inner side of the coating, suggesting the composition depicted in Figure 4c. In this model Li is distributed homogeneously throughout the coating and the alkylation degree of Si increases from the inner to the outer side of the coating.

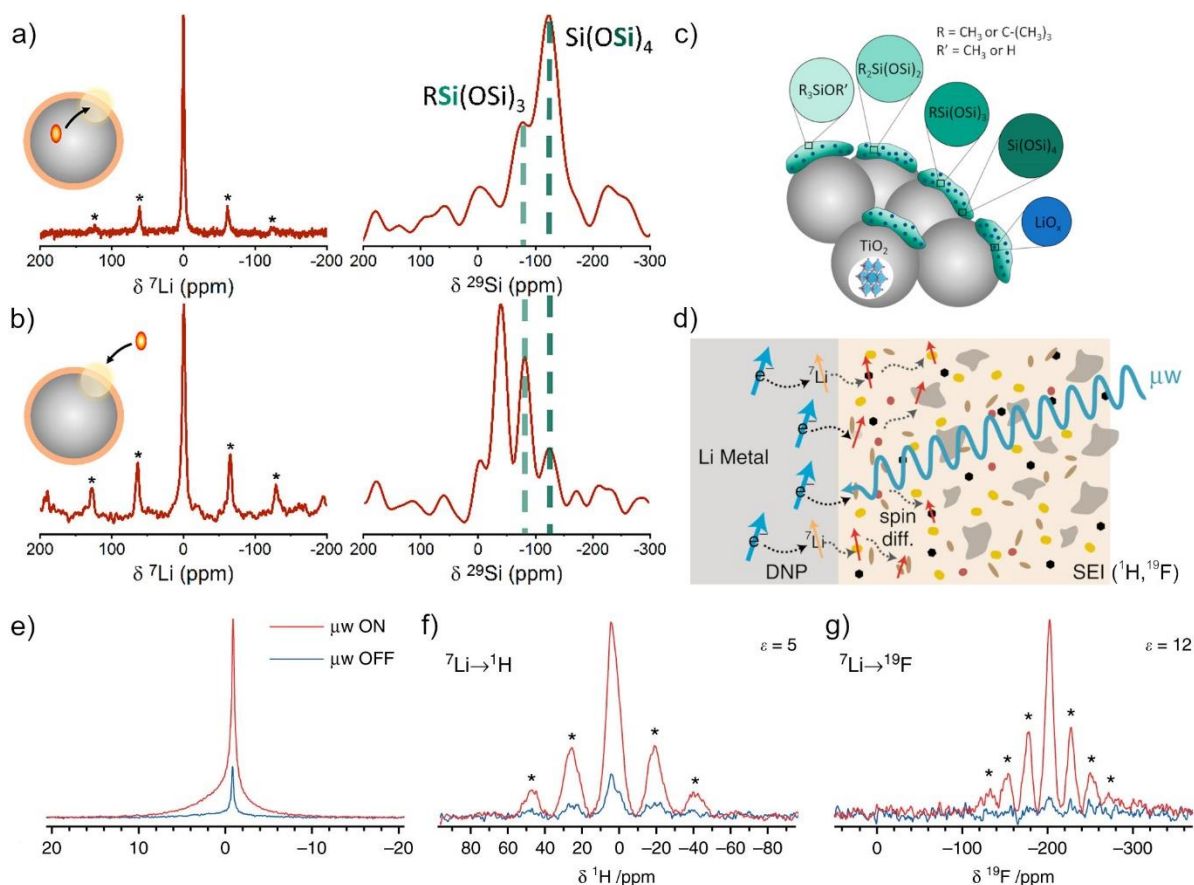


Figure 4. DNP approaches to study coatings at 100 K (a-c) and SEI of Li metal at room temperature (d-g). (a-c) Direct polarization  $^{7}\text{Li}$  and  $^{29}\text{Si}$  spectra enhanced by DNP with (a) the iron dopant (endogenous MIDNP, inner side of the  $\text{TiO}_2$  coating) or with (b) the nitroxide solution (exogenous DNP, outer side of the coating). The polarization source is represented as a red ellipse in the insets. Silica groups (dark green) are the most intense in the  $^{29}\text{Si}$  DNP-NMR spectra of the inner side while alkylated silicon atoms (light green) appear in higher proportion in the outer side. (c) Structural model of the  $\text{Li}_x\text{Si}_y\text{O}_z$  coating layer showing the preferential location of the alkylated silicon and silica environments. Uniformly distributed  $\text{LiO}_x$  is shown in blue. (d) Diagram of the Li metal-SEI interface showing the DNP enhancement process for metallic Li. (e)  $^{7}\text{Li}$  NMR spectra of the diamagnetic SEI in contact with Li microstructures, produced by cycling with the LP30 + FEC electrolyte and recorded with and without microwave irradiation ( $\mu\text{w}$  ON/OFF). (f, g)  $^1\text{H}$  and  $^{19}\text{F}$  spectra obtained by CP-MAS from  $^{7}\text{Li}$ , recorded with and without DNP enhancement. The signals of the protonated and fluorinated environments near Li atoms is specifically enhanced in the proximity of the metallic Li interface and provides easier detection for fluorinated species (LiF based on the  $^{19}\text{F}$  shift) or easier assignment for the more complex  $^1\text{H}$  spectrum. Spinning sidebands are marked with asterisks. Adapted from [18]\*\*, CC-BY licence for (a-c) and adapted from [28], CC-BY-4.0 licence for (d-g).

## 2.2. Challenges related to conductive materials for exogenous DNP

The specificities of exogenous DNP should not be forgotten: low temperature and microwave irradiation. In 2019, a careful study of the effect of conductivity on exogenous DNP studies

was performed on graphite and carbonized carbons [54]. The main detrimental effect of conductivity was identified as a lower polarization transfer from electron to nucleus: a lower electron polarization (local heating) and a lower microwave power efficiency, both due to microwave absorption by the sample. Enhanced relaxation of the radicals could be ruled out. The authors suggested a pulse-DNP approach to lower the heating issues and reach interesting signal enhancements.

### 2.3. Metallic Li solid-electrolyte interface

For lithium-metal batteries, there is another way to reach spatial selectivity of DNP for the interphase: hyperpolarize specifically the foil of metallic Li acting as the negative electrode, using conduction electrons. Interestingly, the first DNP experiment was performed by Carver and Slichter on metallic lithium [55], using a much lower field. Hope et al. [28] obtained such hyperpolarization of the Li atoms in the metal (Overhauser effect between the conducting electrons and the Li atoms) extracted from charged or discharged cells and used the hyperpolarized signal as a starting point to enhance the signal of nearby atoms - bringing in spatial selectivity from the inner side of the SEI (Figure 4d-g).  $^7\text{Li}$ ,  $^1\text{H}$  and  $^{19}\text{F}$  enhanced spectra were analyzed to compare the SEI components in regular LP30 electrolyte and LP30 electrolyte with FEC additive (10%vol). LiF was found in greater amount for the FEC-containing electrolyte, while it was completely absent from the direct  $^{19}\text{F}$  MAS NMR spectrum. One of the main advantages of this approach is the ability to work at room temperature. This is not possible for exogenous DNP as the radical solution must be frozen to ensure proper magnetization transfer.

## 3. *In situ* NMR spectroscopy

*In situ* NMR is essential to study reactions in the full battery environment, without disturbing the electrolyte-electrode interface by extraction. Quantifying inactive Li species in high-energy density Li-ion batteries is crucial to understand degradation and failure mechanisms.

As mentioned in the introduction, *in situ* NMR is a good technique to observe highly reactive species in real time. Studies have concentrated on questions that can be answered despite the lower resolution pertaining to static samples: mainly Li or Na plating, easily separated from the other Li-containing compounds thanks to their large Knight shifts. For *in situ* liquid-state NMR studies of the electrolyte decomposition products the reader is referred to another review [51].

The main interest in recent work has been the characterization of the morphology and quantification of the electrodeposition (reduction of  $\text{Li}^+$ ) of metallic Li, either as the planned reaction or as a parasitic reaction. Quantification in NMR is performed assuming that the area of each  $^7\text{Li}$  NMR peak is proportional to the number of spins in the corresponding environment. This is true for a perfectly homogeneous and electronically insulating sample but challenging for a conductive material, especially in the inhomogeneous environment of a battery.

One should recall here that conductors repel time-dependent (radio-frequency) magnetic fields, so that the ability to measure the NMR spins decays exponentially from the surface with a characteristic length, the skin depth. It depends on the conductivity of the metal and the

frequency of the RF field carrier. As an example, the signal of a thick metallic Li foil (such as an electrode) is not fully proportional to the number of lithium atoms contained, but rather to its surface - the centre is a blind zone.

Most publications focus on the quantification with the *in situ* NMR approach of the amount of plated Li. Most of the time the morphology of the deposited Li is mossy/filamentous or dendritic (high surface area lithium, HSAL), so that the size of the deposited structures is usually assumed to be much smaller than the skin depth of the conductor (17  $\mu\text{m}$  at 4.7 T for metallic Li). Under this condition only can the NMR spectrum integration provide a proper quantification.

### 3.1. Metallic Li electrode and anode-free Cu electrode

Gunnarsdottir et al. explored in 2020 the effect of adding fluoroethylene carbonate (FEC) in the standard LP30 electrolyte and of pulsed current on the processes of SEI formation and of Li electrodeposition, in symmetric Li//Li cells using *in situ* NMR [23]\*\*.

The mass of electrodeposited Li obtained by  $^7\text{Li}$  *in situ* NMR was compared to the mass expected from the electrochemical charge transferred between the electrodes (coulometry) to identify the sources of capacity loss, using *ex situ* Scanning Electron Microscopy (SEM) to confirm. The small change in the metallic  $^7\text{Li}$  intensity for the classical electrolyte was assigned to the formation of dense microstructures, which prevented full quantification of the deposited Li structures (Figure 5a and 5b). This observation differed from previous measurements in their group and it was assigned to the better pressure applied in their *in situ* “capsule” electrochemical cell. With FEC the amounts measured by NMR and coulometry were in better agreement, in line with the assumption of a more porous deposition. The 24% discrepancy was ascribed to SEI formation. An increase in the current further reduced the discrepancy, with formation of even more porous structures together with less SEI formation. Pulsed plating proved to be more effective with or without additive as it delayed the microstructural growth onset.

The metallic Li shift is also sensitive to orientation (250 ppm for a horizontal foil, 260-270 ppm for a vertical foil and HSAL) and it is usually used to separate the contributions of electrodeposited HSAL from the bulk electrode, or to comment on its morphology. Küpers et al. performed a careful monitoring of the lithium deposition by combining electrochemical measurements, *in situ*  $^7\text{Li}$  NMR spectroscopy, and SEM data for different electrolyte compositions and salt concentrations using symmetrical Li//Li thin film pouch cells [38]. Results did not show any substantial changes in the  $^7\text{Li}$  NMR chemical shifts even though ‘smooth’ electrodeposited lithium was detected from SEM images. This highlights the challenges associated with the determination of the amount and the morphology of the electrodeposited lithium, if based on the shift only.

Hsieh et al. published another careful study [39]\* that focused on a protocol combining *in situ* and *ex situ* (static) NMR measurements for more precise quantification of irreversible Li losses in batteries (dead Li, SEI, mossy Li). They validated it using titration gas chromatography (GC) using  $\text{H}_2\text{O} + \text{Li}_{\text{dead}} \rightarrow \text{LiOH} + \text{H}_2$ , with  $\text{H}_2$  quantified by GC, and applied it to distinguish between two processes of capacity loss for Cu//Li cells: “dead” Li (electronically disconnected)

and SEI formation. The amount of dead Li could not be measured by *in situ* NMR as the metallic Li signal remaining at full discharge arises from dead Li on the copper foil and from structures plated on the Li foil, hence the *ex situ* measurements on each electrode. The SEI is hidden in the liquid electrolyte peak and was derived from the coulombic inefficiency and the dead Li quantification. In a follow-up study [33], Hsieh et al. investigated the effect of electrolyte additives (FEC and LiPO<sub>2</sub>F<sub>2</sub>) on lithium deposition and dendrite formation. They compared the alkyl carbonate electrolyte (1M LiPF<sub>6</sub> in EC:DEC 3:7) with and without additives, using different electrodes (Li||Li symmetric cells, Li||Cu, Cu||NMC, and NMC||Li cells). The amount of dead Li and of Li lost in the SEI was quantified using the same protocol. These measurements highlighted the formation of a better and thinner SEI for the dual additives in that electrolyte.

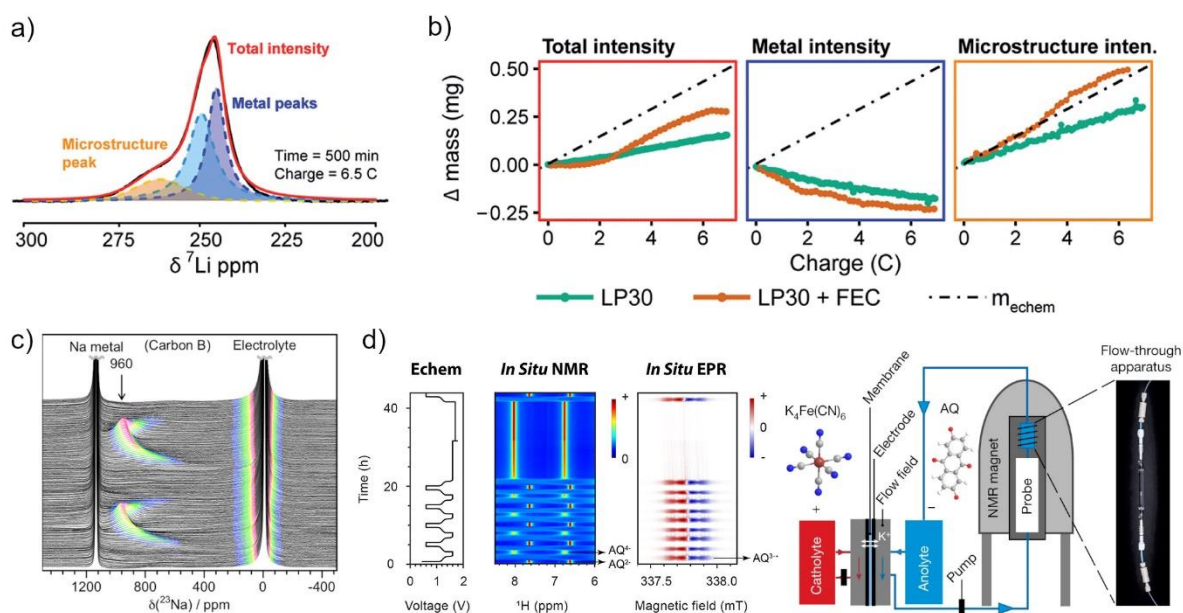


Figure 5. Examples of *in situ* NMR studies for metallic Li plating and hard carbon sodiation. (a) Example of *in situ* <sup>7</sup>Li NMR spectrum obtained for a symmetric Li || Li electrochemical cell polarized for 500 min under a constant current of 0.5 mA cm<sup>-2</sup> in LP30. The simulation into two overlapping metal peaks and one microstructural peak is shown as dashed color-filled peaks. (b) The variation in total, metal and microstructure integrated NMR intensity, converted into a mass change (mg) for cells polarized in LP30 (green) and LP30 + FEC (orange). The differences with the dashed line (deposited mass calculated based on the electrochemistry, assuming no side reaction) indicates a slight loss of intensity due to a smoothing of the Li surface (less metal signal) for the two types of cell. Microstructures are quantitatively detected in the cell with LP30+FEC while the cell with classical LP30 demonstrates a deviation, most probably due to SEI formation. (c) *Operando* <sup>23</sup>Na NMR spectra for an electrochemical cell with sodium metal and hard carbon electrode, and a NaPF<sub>6</sub> electrolyte. Strong features corresponding largely to the electrolyte or Na metal have been truncated for clarity. Spectra are colored in the region -200–1000 ppm according to their intensity. The maximum shift for the spectrum following complete sodium insertion is indicated. The corresponding electrochemistry is shown on the right-hand side. The cell was cycled at a rate of C/20 (achieving a capacity of 300 mAhg<sup>-1</sup> in 20 h) between 2 and 0.005 V, and held at the end of each discharge until the current dropped to below C/100. The hard carbon used was a commercial carbon. (d) The on-line setup for *in situ* studies of redox-flow batteries. Here the

battery comprises 5.0 cm<sup>2</sup> carbon felt electrodes, with a catholyte and an anolyte of potassium ferrocyanide(II) and 2,6-dihydroxyanthraquinone, respectively, dissolved in 1 M KOH in D<sub>2</sub>O. Part of the anolyte flows through the NMR and EPR magnet at a flow rate of 13.6 cm<sup>3</sup> min<sup>-1</sup>. The NMR and EPR spectra enables the species formed upon reduction and the rate constants of the various processes to be determined.

Adapted for (a-b) from [23]\*\* (CC-BY 3.0 licence), for (c) adapted from [48]\* (CC BY 4.0 licence) and for (d) adapted from [49] (copyright © 2020, The Author(s), under exclusive licence to Springer Nature Limited) and from [50] (CC BY licence).

In another study [40] by Gunnarsdóttir et al. in 2020, *in situ* <sup>7</sup>Li NMR was performed to investigate the performance of three electrolyte formulations in an anode-free LiFePO<sub>4</sub>//Cu cell: LP30, LP30+FEC and 1 M LiTFSI in 1,3-dioxolane:1,2-dimethoxyether (DOL:DME, 1 :1) + 2% LiNO<sub>3</sub>. Dead lithium was quantified by *in situ* <sup>7</sup>Li NMR and compared with the coulombic efficiency to deduce the amount of SEI formation. LP30+FEC was the best electrolyte among the three studied, with the lowest amounts of SEI and dead lithium formation. Interestingly, the metallic Li peak position was influenced by the magnetic susceptibility of the LiFePO<sub>4</sub> electrode, so that the interpretation of the NMR shift in terms of Li morphology had to be corrected before comparison with other studies. Changes in shift were however observed after that correction and they were discussed in terms of better Cu coverage and dead Li formation. Finally, Li corrosion (dissolution) was investigated in a fully charged cell, left in open circuit (no current). LP30+FEC was again found to be better with lower Li dissolution as measured by following the metallic <sup>7</sup>Li NMR peak. Polymer coating of Cu also demonstrated a better Li stability in open circuit, which meant that “sacrificial” corrosion of Li on Cu was not negligible. Menkin et al. used the same *in situ* approach, in combination with the *ex situ* measurements mentioned in section 1.1, to study the influence of the initial acidic treatment of the Cu surface on the Li plating and Li loss mechanisms [13]. Dead Li was observed in all cases and a non-negligible galvanic corrosion process with Cu was necessary to explain the Li intensity changes upon cycling.

A similar strategy was also conducted by Xiang et al. on a LiFePO<sub>4</sub>//Cu anode-free battery to analyse its failure modes [41]. Dead Li was quantified by *operando* <sup>7</sup>Li NMR and SEI formation assumed to be the remaining source of capacity loss. SEI formation was initially dominant and after the 3<sup>rd</sup> cycle SEI and dead Li contributed in equal part to the cell's failure. This balance is tilted towards Li consumption by SEI when the FEC additive is used, while dead Li is the main culprit for cell failure at higher rates. Discrepancies with titration gas chromatography were interpreted in terms of LiH formation on dead Li and further confirmed using mass spectrometry titration with D<sub>2</sub>O (D<sub>2</sub>O+Li<sub>dead</sub> → LiOD+ ½ D<sub>2</sub>; D<sub>2</sub>O+LiH → LiOD+1/2 HD). 1 M LiTFSI in 1,3-dioxolane:1,2-dimethoxyether (DOL:DME, 1 :1) + 2% LiNO<sub>3</sub>. The interesting question of the detection limit was also discussed – with their experimental setup the limit of detection by NMR was lower than 3.9 µg.

Wang et al. tried to enhance Li metal stripping/plating efficiencies using a high dielectric BaTiO<sub>3</sub> porous scaffold. This scaffold was meant to reduce the large electrical field gradients present on the surface inhomogeneities of metallic Li and limit dendrite and dead Li formation in “anode-less“/LiCoO<sub>2</sub> cells [42]. *Operando* <sup>7</sup>Li NMR revealed that this scaffold promoted dense Li deposition and limited the formation of dead Li compared to bare Cu.

Another approach of interest was used by Gunnarsdottir et al. [23]\*\* to probe the exchanges through the SEI. These were probed using tracer-exchange  $^6\text{Li}/^7\text{Li}$  NMR to identify the mobility across the Li-electrolyte interface at equilibrium (no net current).  $^6\text{Li}$ -enriched metallic foils were soaked in an NMR tube with the natural abundance  $^7\text{Li}$ -rich electrolytes under study (LP30 or LP30+FEC). *In situ*  $^7\text{Li}$  NMR measurements gave an indication of the amount of  $^7\text{Li}$  atoms exchanged between the electrolyte and SEI (initially 93%  $^7\text{Li}$ ) to the metallic electrode (initially 95%  $^6\text{Li}$ ). FEC was demonstrated to enhance the rate of SEI formation and to provide a more dynamical interface, so that the lithium concentrations on the surface of metallic Li were more homogeneous, hence diminishing the risk of dendrite formation.

### 3.2. Plating on graphite in full cells

One of the detrimental side reactions occurring on the negative electrode upon charging is the direct deposition of lithium as metal rather than its insertion into the graphite electrode, which results in premature ageing of the cell. Signatures of Li-plating can be detected in the electrochemical behaviour of the cell in the following charge, but it is extremely challenging to detect small quantities in real time.  $^7\text{Li}$  *operando* NMR has been extensively exploited in recent years for that purpose.

Krachkovskiy et al. developed a parallel-plate NMR resonator for *in situ*  $^7\text{Li}$  NMR measurements of “cartridge-like” (prismatic) Li-ion batteries. The authors proposed a quantification method that they applied to a home-made NMC622//graphite parallel-plate cell, using electrodes harvested from a commercial cell [43]. The electrode/electrolyte/electrode assembly was sandwiched between the Cu plates of the resonator and the ensemble was sealed for air-tightness. Slow charge (C/4, full charge in 4 h) was compared to faster charge (1C, full charge in 1 h) using 8 intermediate steps of the charge in open circuit conditions.

Li metal deposition on the graphite was quantified assuming proportionality between the area of the corresponding  $^7\text{Li}$  NMR peak and the amount of deposit. We recall that in the following the deposits are assumed to have morphologies smaller than the skin-depth of the RF field for  $^7\text{Li}$  so that the whole of the deposit can be quantified. The graphite state-of-charge was evaluated using its central line in the  $^7\text{Li}$  NMR spectrum. Issues associated with changes in graphite conductivity were also considered as negligible in that case.

A fraction of the plated lithium was shown to reintercalate into graphite (chemical reaction) as the current was turned off. It was deduced from the  $^7\text{Li}$  NMR shifts that Li reintercalation into graphite was mainly happening from the flat film of Li deposited on the surface, while the lithium deposited as dendrites could partially “dissolve” into the electrolyte solution during the subsequent discharge of the cell.

An improved cartridge electrochemical cell and resonator were designed by Aguilera et al. [32] and then Sanders et al. to perform *operando*  $^7\text{Li}$  NMR measurement on an NMC622//graphite cell [44]. The resonator and electrochemical cell were separated to enable easier battery assembly and reproducibility, which is then slid inside the resonator. Metallic Li deposition was detected in fast charge conditions (1C) above 4 V and during the constant voltage step at 4.25 V at the end of charge. While some of the deposited Li metal intercalated into graphite during the subsequent open-circuit step, a fraction of Li metal, considered as “dead Li”, was not oxidized during the subsequent slow (C/5) discharges. It was hypothesized that these disconnected Li added a layer at each cycle onto the graphite surface, separated from the former Li layer by insulating SEI. This would create a barrier for  $\text{Li}^+$  transport, reduce the

intercalation rate into graphite during open-circuit and contribute to the formation of dead Li as an extra layer.

Li plating was also characterized on NMC811/graphite cells as a function of temperature and charging rate by Märker et al. [45]\*. Low amounts of Li-plating and re-intercalation into graphite were also observed and linked to kinetic limitations. Interestingly, the authors mentioned that self-standing electrodes did not behave properly compared to films deposited on a Cu current collector, highlighting the need for careful preparation of the cells when studying small quantities created by side-reactions.

Afonso de Araujo et al. (submitted) concentrated on low-temperature measurements of Li plating in NMC622/graphite batteries [46]. A specific *in situ* probe setup with a “cylindrical” cell, using a geometry similar to a coin cell, was developed to reach -20°C with stronger pressure applied to the assembled cell compared to pouch cell. This was necessary to obtain more reproducible electrochemistry. The experimental setup and analysis were pushed to increase the limit of detection for metallic Li to identify at the earliest the onset of Li deposition as a function of charging rate and temperature, and its evolution upon resting in open circuit.

### 3.3. Na-ion batteries

Regarding the deposition of metallic Na, the reports on *in situ*  $^{23}\text{Na}$  NMR spectroscopy from the last years focused on the effect of additives in the electrolyte or on the characterization of sodium deposition on the surface of the negative hard carbon electrode. Two mechanisms are considered: sodium “pooling” with the formation of Na clusters in the pores near the carbon surface, or more classical Na intercalation in the ordered layers of hard carbon.

Bray et al. employed operando  $^{23}\text{Na}$  NMR spectroscopy to study the processes in a full cell [36]. A full cell ( $\text{NaNi}_{1/3}\text{Fe}_{1/3}\text{Mn}_{1/12}\text{Sn}_{1/12}\text{O}_2$ //hard carbon) was characterized to make sure that the signature observed in the 1130 ppm region would only arise from plating on the surface of hard carbon and not from a metallic Na electrode. Two types of signal were observed: the first appears near the typical shift of metallic Na (~1100 ppm) and disappears quickly (seen between 1.5 h and 2.h charging over a ~6 h charge), while the second one appears later in a region assigned to quasi-metallic Na clusters in the carbon pores (~400 ppm), and disappears upon discharge. No Na plating was observed at full charge.

The mechanism of oversodiation was investigated by Gotoh et al. for half cells (hard carbon//Na) using *operando* and *ex-situ*  $^{23}\text{Na}$  NMR [47]. Oversodiation of hard carbon resulted in metallic Na and dendrites near 1120-1130 ppm in the *operando*  $^{23}\text{Na}$  NMR spectra. The disagreement of the shift compared to the report by Bray et al. most probably comes from different susceptibility effects (the electrodes are perpendicular to the main magnetic field here, while they were parallel for Bray et al). The signature for quasi-metallic sodium was not observed *operando*, but it was present in *ex situ*  $^{23}\text{Na}$  MAS-NMR measurements (near 1100 ppm) at the end of charge.

Stratford et al. also published a report on half-cells (hard carbon//Na) comparing four types of hard carbons with differing pore size and correlation length of their graphene layers [48]\*. The

range of shift for the sodiated carbon was 760 to 960 ppm (Figure 5c), indicating increased metallicity of the Na “clusters”. This study highlighted the sensitivity of the Knight shift to both Na cluster size (as derived by SAXS/SANS) and carbon structural order (from pair-distribution function analysis), and stressed the need for an array of complementary techniques to reach a full understanding of the factors influencing Na plating in hard carbon.

Finally, Xiang et al. used  $^{23}\text{Na}$  *in situ* NMR spectroscopy to analyse the effect on Na deposition by the FEC additive in a Na//Na symmetric battery [29]. The electrolyte was slightly different: 1 M  $\text{NaClO}_4$  in PC electrolyte. The constant area of the signal of metallic sodium at 1125 ppm indicated a constant surface area and thus smooth deposition with the FEC additive, while a drastic increase was observed for the same electrolyte without additive, assigned to mossy microstructure deposited on the Na electrode. This was linked with the strong electrolyte decomposition observed from *ex situ*  $^{23}\text{Na}$  NMR measurements on Na//Cu cells (section 1.4).

### 3.4. Redox-flow

Redox-flow batteries have a very different design that brings opportunities for NMR measurements. They are based on liquids containing the positive electrode (catholyte) and the negative electrode (anolyte). These are stored in separate reservoirs and they are brought into contact for reaction through a circulation from each reservoir to a flow cell (with a separator to prevent direct redox reaction and wires to enable electron exchange).

In 2020, Zhao et al. [49] demonstrated two approaches: in-line NMR on the anolyte circulating between the reservoir and the flow cell (Figure 5d) and an *in situ* approach by including the flow cell into the NMR probe. Both approaches rely on measuring the liquid-state NMR signal and enabled the characterization of the state of charge of the 2,6-dihydroxyanthraquinone (DHAQ) and 4,4'-((9,10-anthraquinone-2,6-diyl)dioxy)dibutyrates (DBEAQ) in a 1M KOH in  $\text{D}_2\text{O}$  electrolyte. The  $^1\text{H}$  NMR shifts are modified (disappearance or change in shift by  $\sim 1$  ppm) as the redox state of the quinone changes: unpaired electrons appear on the quinone redox centres. The shift of the peak from the partially protonated water signal is also an indicator of magnetic susceptibility changes linked directly to the state-of-charge of the redox-flow battery. This approach enabled the determination of the mechanism for the electrochemical reactions, and a model was developed to extract the equilibrium constants between the two reduced forms of the two catholytes. The *in situ* measurements also enabled the observation of the decomposition products from the reduced forms of the catholyte (such as anthrone and anthrol) and their dependence with the voltage plateau on top of charge. Finally, self-discharge through side reactions (reoxidation of  $\text{DBEAQ}^{4-}$ , hydrogen evolution) could also be characterized with the *in situ* NMR setup.

In a follow-up study, in-line Electron Paramagnetic Resonance (EPR) was coupled to the existing in-line  $^1\text{H}$  NMR spectroscopy [50]. EPR and NMR are highly complementary as the former is blind to diamagnetic species while the second is blind to paramagnetic species. Hence the radical intermediate is detected by EPR while the NMR detects the non-radical quinones. Combining the high sensitivity of EPR for radicals to NMR confirmed the previous results and enabled a more precise determination of the rate of exchange for electrons in the intermediate redox species (Figure 5d).

## 4. *In situ* imaging and spatial-dependent information

The ability to localize spatially the signals is another asset of magnetic resonance. Magnetic field gradients modulate the NMR frequency according to the position in the gradient of the NMR-active atom. It therefore provides a mean to locate the spins with a precision around  $1\ \mu\text{m}$  in the best cases for  $^1\text{H}$  Magnetic Resonance Imaging (MRI), down to a few  $100\ \mu\text{m}$  in most cases. The challenge is the resolution that requires strong magnetic field gradients and long signal living times. Most recent *in situ* studies concentrate therefore on the liquid electrolyte. One of the main assets of MRI is the chemical selectivity – only one type of atom is used to generate the image - and the ability to obtain localized spectroscopic parameters.

### 4.1. Electrolyte under polarization

The liquid electrolyte is the easiest part to image thanks to its long relaxation times and images were recorded for cells with artificially enhanced separation (a few mm) between electrodes for resolution issues. Recently, Goward and co-workers [30]\* used a combination of pulsed-field gradient (PFG) techniques and MRI to determine, in the context of Li plating inside graphite//Li cell, localized electrolyte transport properties at varying temperatures and currents. Using  $^7\text{Li}$  and  $^{19}\text{F}$  NMR to follow the cations and anions of the  $\text{LiPF}_6$  electrolytic salt, localized self-diffusivities and concentrations were measured across the electrolyte, under a given driving current and in the steady state and with a resolution close to  $200\ \mu\text{m}$  (for an electrolyte thickness of  $2\ \text{mm}$ ). These confirmed that the depletion of  $\text{Li}^+$  ions at the cathodic side is the limiting factor at room temperature. On the other hand, at low temperature, the anodic side appeared as diffusion limited, against expectations.

Other localized NMR observables, such as transverse relaxation rates, can also be measured for the electrolyte, with a resolution approaching  $200\ \mu\text{m}$ . In that case, the electrochemical cell was made of NMC / $\text{LiPF}_6$  1M in EC:DMC 1:1/graphite, assembled with an extremely thick separator (12 layers,  $10\ \text{mm}$ ). The transverse relaxation rate of  $^7\text{Li}$  in the liquid electrolyte was monitored in open circuit conditions and indicated an increase in relaxivity. This behaviour was assigned to Ni dissolution from the positive electrode. Electrolyte decomposition was also envisaged owing to the reversal in the cell polarity. [31]

The previous measurements used the traditional design of a “Swagelok cell” placed vertically in a  $10\ \text{mm}$  saddle coil. In this kind of cell, the electrodes and separators are disks pressed against each other within a cylindrical plastic container, which mirrors coin cell behaviour.

The other approach developed by Balcom and co-workers consists in using a geometry that is compatible with the pouch (or prismatic) design [32]. In that case, the electrolyte concentration profile between electrodes separated by  $1\ \text{mm}$  could be measured in an NMC532//graphite battery. But the novelty resides in the approach, relatively common in the MRI field (although not localized), of correlating longitudinal and transversal relaxation rates to discriminate the components. In this study, two couples of ( $T_1$ ,  $T_2$ ) values were obtained for the electrolyte between the electrodes. They could be separated from Li in the graphite pores, Li intercalated in graphite and metallic Li based on their characteristics. This approach is of special interest when the chemical shift information is not retrievable, for example because of a low field magnet or because of strong distortions due to conductive parts in the battery.

The measurement of the electrolyte concentration in electroactive ions is also a way to follow the impact of additives on the behaviour of Li plating in lithium metal batteries. Hsieh et al. [33] observed by  $^{19}\text{F}$  MRI using symmetric Li//Li pouch cells that additives such as 2% FEC (fluoroethylene carbonate) and 1%  $\text{LiPO}_2\text{F}_2$  (flame retardant) reduced the concentration gradients of anions within the electrolyte and anion depletion on the plating electrode, hence delaying the onset of lithium plating.

## 4.2. Li plating and solid electrolyte

Solid electrolytes are sought after to eliminate the alkyl carbonate solvents that bring a risk of inflammation following a short-circuit. A report from Marbella et al. [34] in 2019 used chemical shift imaging (CSI) to get spatial information about Li growth through the solid electrolyte in Li/LLZTO ( $\text{Li}_{6.5}\text{La}_3\text{Zr}_{1.5}\text{Ta}_{0.5}\text{O}_{12}$ )/Li symmetrical cells. The CSI experiment correlates the  $^7\text{Li}$  NMR spectrum with the position. Such correlation maps provide enough resolution (300  $\mu\text{m}$  for an electrolyte thickness of 2.5 mm) to identify Li deposition in the cell. At early times a slightly sloping voltage could be related to dense Li deposition on the surface of the Li electrodes, corroborated by SEM measurements. Although the resolution is low, the specific chemical shift for metallic lithium enables its selective observation throughout the cell, and could provide a potential diagnosis tool for the early stages of lithium deposition.

## 4.3. Na microstructures

$^{23}\text{Na}$  MRI is more challenging than  $^7\text{Li}$  due to a faster quadrupolar relaxation, but a few studies have been published recently that work on characterising sodium microstructures after plating. *Operando* MRI is not feasible owing to the long measurement times. Metallic sodium has relatively longer relaxation times compared to other sodium species and low-resolution images can be obtained (250-1000  $\mu\text{m}$ ).

Xiang et al. combined imaging and spectroscopy to correlate the spectrum with the location (localized spectroscopy) in anode-free Na//Cu batteries [29]. They identified a strong reversibility of Na plating on Cu when the electrolyte contained the additive fluoroethylene carbonate (FEC), with no  $^{23}\text{Na}$  signal for metallic Na on the Cu electrode after a charge-discharge cycle. The reference electrolyte, 1 M  $\text{NaClO}_4$  in PC, demonstrated “dead Na” left near the surface of the Cu electrode after one cycle. This “dead” Na accumulated on the Cu electrode as more and more side reactions proceeded. They linked it to the overpotential increase as the cell is ageing, and validated their hypothesis using *in situ* NMR spectroscopy of the metallic Na signal.

Rees et al. also used the  $^{23}\text{Na}$  signal to image Na microstructures grown in an all-solid-state cell with two Na electrodes and a ceramic solid electrolyte cycled under 1 MPa [35]\*. They demonstrated that, although resolution is relatively poor, the contrast based on the transverse relaxation time (intensity of pixel governed by  $T_2$  relaxation rather than just Na concentration) highlighted the Na microstructures, thanks to a higher mobility of the Na ions in these structures (Figure 6).

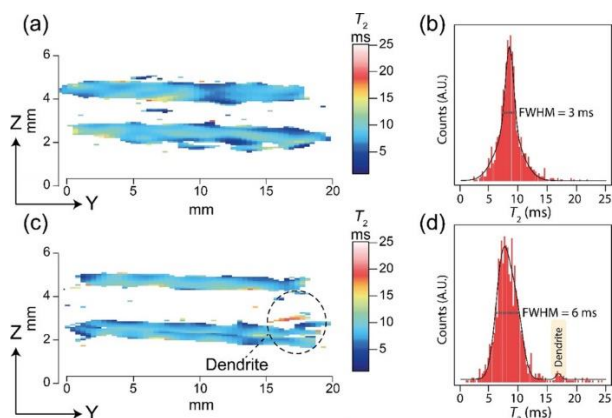


Figure 6. The  $T_2$  weighted contrast maps of a) the pristine symmetrical Na/Na- $\beta$ "-Alumina/Na cell and c) the cell polarized in the same direction for 19 h under a pressure of 1 MPa, followed by a current reversal and instantaneous short-circuit. The  $T_2$  distributions were obtained from 5 spin-echo images with echo durations ranging from 2 to 12 ms. A specific microstructure, assigned to dendrite by the authors, is highlighted and has a significantly increased  $T_2$ , around 16 ms. The respective total  $T_2$  distributions are given in the histograms (b) and (d), with the isolated dendrite distribution highlighted. Reproduced from [35], CC BY licence.

Finally, Bray et al. [36] focused on a half cell with hard carbon as the working electrode and metallic sodium as the counter electrode, with a liquid electrolyte (NaPF<sub>6</sub> 1 M in EC/DMC). They recorded the negative of the Na microstructures deposited on graphite during discharge, using the <sup>1</sup>H 3D-image of the electrolyte in which the Na microstructures appear as black (no signal). This smart trick was introduced earlier to enhance resolution in the study of Li plating in Li//Li cells [56].

## Conclusions

NMR is traditionally not a routine characterization tool in the field of rechargeable batteries. Recently, the ability to selectively address the interfaces, through chemical or spatial selectivity has triggered a lot of interest. One of the main assets exploited in the last years was the quantification in *ex situ* MAS-NMR studies of the SEI and *in situ* NMR studies of Li or Na plating. This ability is powerful, but it should be exploited with care as several conditions must be fulfilled for the measurements to be accurate. The development of DNP for sensitivity and MRI for spatially localized information should also result in a continued progress of NMR implementation in the battery field in the future.

## Funding

This work was supported by the French CNRS; the Agence Nationale de la Recherche (ANR) [LABEX STORE-EX (ANR-10-LABX-76)]; and the University of Orléans [PhD grant].

# Bibliography

- [1] X. Liu, Z. Liang, Y. Xiang, M. Lin, Q. Li, Z. Liu, G. Zhong, R. Fu, Y. Yang, Solid-State NMR and MRI Spectroscopy for Li/Na Batteries: Materials, Interface, and In Situ Characterization, *Advanced Materials*. 33 (2021) 2005878. <https://doi.org/10.1002/adma.202005878>.
- [2] K. Gotoh, 23Na Solid-State NMR Analyses for Na-Ion Batteries and Materials, *Batteries & Supercaps*. 4 (2021) 1267–1278. <https://doi.org/10.1002/batt.202000295>.
- [3] K.S. Han, J.D. Bazak, Y. Chen, T.R. Graham, N.M. Washton, J.Z. Hu, V. Murugesan, K.T. Mueller, Pulsed Field Gradient Nuclear Magnetic Resonance and Diffusion Analysis in Battery Research, *Chem. Mater*. 33 (2021) 8562–8590. <https://doi.org/10.1021/acs.chemmater.1c02891>.
- [4] K. Hogrefe, N. Minafra, W.G. Zeier, H.M.R. Wilkening, Tracking Ions the Direct Way: Long-Range Li<sup>+</sup> Dynamics in the Thio-LISICON Family Li<sub>4</sub>MCh<sub>4</sub> (M = Sn, Ge; Ch = S, Se) as Probed by <sup>7</sup>Li NMR Relaxometry and <sup>7</sup>Li Spin-Alignment Echo NMR, *J. Phys. Chem. C*. 125 (2021) 2306–2317. <https://doi.org/10.1021/acs.jpcc.0c10224>.
- [5] C.C. Fraenza, S.G. Greenbaum, Broadband NMR relaxometry of electrolytes for energy storage, *Chem. Phys. Rev*. 3 (2022) 011307. <https://doi.org/10.1063/5.0076580>.
- [6] S. Haber, M. Leskes, What Can We Learn from Solid State NMR on the Electrode-Electrolyte Interface?, *Adv. Mater*. 30 (2018) 1706496. <https://doi.org/10.1002/adma.201706496>.
- [7] B. Han, C. Liao, F. Dogan, S.E. Trask, S.H. Lapidus, J.T. Vaughey, B. Key, Using Mixed Salt Electrolytes to Stabilize Silicon Anodes for Lithium-Ion Batteries via in Situ Formation of Li–M–Si Ternaries (M = Mg, Zn, Al, Ca), *ACS Appl. Mater. Interfaces*. 11 (2019) 29780–29790. <https://doi.org/10.1021/acsami.9b07270>.
- \*[8] K. Arano, S. Begic, F. Chen, D. Rakov, D. Mazouzi, N. Gautier, R. Kerr, B. Lestriez, J. Le Bideau, P.C. Howlett, D. Guyomard, M. Forsyth, N. Dupre, Tuning the Formation and Structure of the Silicon Electrode/Ionic Liquid Electrolyte Interphase in Superconcentrated Ionic Liquids, *ACS Appl. Mater. Interfaces*. 13 (2021) 28281–28294. <https://doi.org/10.1021/acsami.1c06465>.  
Typical example of quantification of the Li amount in the SEI of Silicon using *ex situ* <sup>7</sup>Li and <sup>19</sup>F MAS NMR and calibration curves.
- [9] J. Xiong, N. Dupré, D. Mazouzi, D. Guyomard, L. Roué, B. Lestriez, Influence of the Polyacrylic Acid Binder Neutralization Degree on the Initial Electrochemical Behavior of a Silicon/Graphite Electrode, *ACS Appl. Mater. Interfaces*. 13 (2021) 28304–28323. <https://doi.org/10.1021/acsami.1c06683>.
- [10] R. May, K.J. Fritzsche, D. Livitz, S.R. Denny, L.E. Marbella, Rapid Interfacial Exchange of Li Ions Dictates High Coulombic Efficiency in Li Metal Anodes, *ACS Energy Letters*. (2021). <https://doi.org/10.1021/acsenergylett.1c00112>.
- [11] R. May, Y. Zhang, S.R. Denny, V. Viswanathan, L.E. Marbella, Leveraging Cation Identity to Engineer Solid Electrolyte Interphases for Rechargeable Lithium Metal Anodes, *Cell Reports Physical Science*. 1 (2020) 100239. <https://doi.org/10.1016/j.xcrp.2020.100239>.
- [12] G. Zheng, Y. Xiang, S. Chen, S. Ganapathy, T.W. Verhallen, M. Liu, G. Zhong, J. Zhu, X. Han, W. Wang, W. Zhao, M. Wagemaker, Y. Yang, Additives synergy for stable interface formation on rechargeable lithium metal anodes, *Energy Storage Materials*. 29 (2020) 377–385. <https://doi.org/10.1016/j.ensm.2019.12.027>.
- [13] S. Menkin, C.A. O’Keefe, A.B. Gunnarsdóttir, S. Dey, F.M. Pesci, Z. Shen, A. Aguadero, C.P. Grey, Toward an Understanding of SEI Formation and Lithium Plating on Copper in Anode-Free Batteries, *J. Phys. Chem. C*. 125 (2021) 16719–16732. <https://doi.org/10.1021/acs.jpcc.1c03877>.
- \*\*[14] M. Liu, S. Ganapathy, M. Wagemaker, A Direct View on Li-Ion Transport and Li-Metal Plating in Inorganic and Hybrid Solid-State Electrolytes, *Acc. Chem. Res*. 55

- (2022) 333–344. <https://doi.org/10.1021/acs.accounts.1c00618>.  
A review of the work of this group on transport in solid electrolytes. Examples of EXSY, tracer-exchange  $^6\text{Li}$  NMR and selective transfers applied to solids.
- [15] P. Wang, H. Liu, S. Patel, X. Feng, P.-H. Chien, Y. Wang, Y.-Y. Hu, Fast Ion Conduction and Its Origin in  $\text{Li}_{6-x}\text{PS}_5-x\text{Br}_{1+x}$ , *Chem. Mater.* 32 (2020) 3833–3840. <https://doi.org/10.1021/acs.chemmater.9b05331>.
- [16] M. Bichon, D. Sotta, N. Dupré, E. De Vito, A. Boulineau, W. Porcher, B. Lestriez, Study of Immersion of  $\text{LiNi}_0.5\text{Mn}_0.3\text{Co}_0.2\text{O}_2$  Material in Water for Aqueous Processing of Positive Electrode for Li-Ion Batteries, *ACS Appl. Mater. Interfaces.* 11 (2019) 18331–18341. <https://doi.org/10.1021/acsami.9b00999>.
- [17] J.C. Hestenes, R. May, J.T. Sadowski, N. Munich, L.E. Marbella, Resolving Chemical and Spatial Heterogeneities at Complex Electrochemical Interfaces in Li-Ion Batteries, *Chem. Mater.* 34 (2022) 232–243. <https://doi.org/10.1021/acs.chemmater.1c03185>.
- \*\*[18] S. Haber, Rosy, A. Saha, O. Brontvein, R. Carmieli, A. Zohar, M. Noked, M. Leskes, Structure and Functionality of an Alkylated  $\text{Li}_x\text{Si}_y\text{O}_z$  Interphase for High-Energy Cathodes from DNP-ssNMR Spectroscopy, *J. Am. Chem. Soc.* 143 (2021) 4694–4704. <https://doi.org/10.1021/jacs.1c00215>.  
Analysis of the structuration of a coated interphase. The study demonstrates the complementarity of exogeneous and endogeneous DNP.
- [19] L. Gao, J. Chen, Q. Chen, X. Kong, The chemical evolution of solid electrolyte interface in sodium metal batteries, *Sci Adv.* 8 (2022) eabm4606. <https://doi.org/10.1126/sciadv.abm4606>.
- [20] J. Sun, L.A. O'Dell, M. Armand, P.C. Howlett, M. Forsyth, Anion-Derived Solid-Electrolyte Interphase Enables Long Life Na-Ion Batteries Using Superconcentrated Ionic Liquid Electrolytes, *ACS Energy Lett.* 6 (2021) 2481–2490. <https://doi.org/10.1021/acsenerylett.1c00816>.
- [21] S.A. Ferdousi, L.A. O'Dell, M. Hilder, A.J. Barlow, M. Armand, M. Forsyth, P.C. Howlett, SEI Formation on Sodium Metal Electrodes in Superconcentrated Ionic Liquid Electrolytes and the Effect of Additive Water, *ACS Appl. Mater. Interfaces.* 13 (2021) 5706–5720. <https://doi.org/10.1021/acsami.0c18119>.
- [22] S.A. Ferdousi, L.A. O'Dell, J. Sun, Y. Hora, M. Forsyth, P.C. Howlett, High-Performance Cycling of Na Metal Anodes in Phosphonium and Pyrrolidinium Fluoro(sulfonyl)imide Based Ionic Liquid Electrolytes, *ACS Appl. Mater. Interfaces.* 14 (2022) 15784–15798. <https://doi.org/10.1021/acsami.1c24812>.
- \*\*[23] A. B. Gunnarsdóttir, S. Vema, S. Menkin, L. E. Marbella, C. P. Grey, Investigating the effect of a fluoroethylene carbonate additive on lithium deposition and the solid electrolyte interphase in lithium metal batteries using in situ NMR spectroscopy, *Journal of Materials Chemistry A.* 8 (2020) 14975–14992. <https://doi.org/10.1039/D0TA05652A>.  
*In situ* measurement of Li exchange across the liquid-solid interface for metallic Li at equilibrium using  $^6,7\text{Li}$  selective isotopic enrichment. A numerical model is developed to extract exchange rates.
- [24] S. Haber, M. Leskes, Dynamic Nuclear Polarization in battery materials, *Solid State Nuclear Magnetic Resonance.* 117 (2022) 101763. <https://doi.org/10.1016/j.ssnmr.2021.101763>.
- [25] I.B. Moroz, M. Leskes, Dynamic Nuclear Polarization Solid-State NMR Spectroscopy for Materials Research, *Annu. Rev. Mater. Res.* 52 (2022) annurev-matsci-081720-085634. <https://doi.org/10.1146/annurev-matsci-081720-085634>.
- [26] J.C. Hestenes, A.W. Ells, M. Navarro Goldaraz, I.V. Sergeev, B. Itin, L.E. Marbella, Reversible Deposition and Stripping of the Cathode Electrolyte Interphase on  $\text{Li}_2\text{RuO}_3$ , *Frontiers in Chemistry.* 8 (2020). <https://doi.org/10.3389/fchem.2020.00681>.
- [27] Rosy, S. Haber, E. Evenstein, A. Saha, O. Brontvein, Y. Kratish, D. Bravo-Zhivotovskii, Y. Apeloig, M. Leskes, M. Noked, Alkylated  $\text{Li}_x\text{Si}_y\text{O}_z$  Coating for Stabilization of Li-rich Layered Oxide Cathodes, *Energy Storage Materials.* 33 (2020) 268–275. <https://doi.org/10.1016/j.ensm.2020.08.015>.

- [28] M.A. Hope, B.L.D. Rinkel, A.B. Gunnarsdóttir, K. Märker, S. Menkin, S. Paul, I.V. Sergeev, C.P. Grey, Selective NMR observation of the SEI–metal interface by dynamic nuclear polarisation from lithium metal, *Nat Commun.* 11 (2020) 2224. <https://doi.org/10.1038/s41467-020-16114-x>.
- [29] Y. Xiang, G. Zheng, Z. Liang, Y. Jin, X. Liu, S. Chen, K. Zhou, J. Zhu, M. Lin, H. He, J. Wan, S. Yu, G. Zhong, R. Fu, Y. Li, Y. Yang, Visualizing the growth process of sodium microstructures in sodium batteries by in-situ  $^{23}\text{Na}$  MRI and NMR spectroscopy, *Nat. Nanotechnol.* 15 (2020) 883–890. <https://doi.org/10.1038/s41565-020-0749-7>.
- \*[30] J.D. Bazak, J.P. Allen, S.A. Krachkovskiy, G.R. Goward, Mapping of Lithium-Ion Battery Electrolyte Transport Properties and Limiting Currents with In Situ MRI, *J. Electrochem. Soc.* 167 (2020) 140518. <https://doi.org/10.1149/1945-7111/abc0c9>. Combination of imaging and localized measurements to determine transport properties in the liquid electrolyte under polarization. This study condenses several years of work.
- [31] R. Balbierer, P. Seegert, S. Herberger, T. Wetzel, H. Nirschl, G. Guthausen, Investigation of Transverse Relaxation Rate Distribution via Magnetic Resonance Imaging: Impact of Electrode Formation, *Energy Technology.* 9 (2021) 2000579. <https://doi.org/10.1002/ente.202000579>.
- [32] A.R. Aguilera, B. MacMillan, S. Krachkovskiy, K.J. Sanders, F. Alkhayri, C. Adam Dyker, G.R. Goward, B.J. Balcom, A parallel-plate RF probe and battery cartridge for  $^7\text{Li}$  ion battery studies, *Journal of Magnetic Resonance.* 325 (2021) 106943. <https://doi.org/10.1016/j.jmr.2021.106943>.
- [33] Y.-C. Hsieh, J.H. Thienenkamp, C.-J. Huang, H.-C. Tao, U. Rodehorst, B.J. Hwang, M. Winter, G. Brunklaus, Revealing the Impact of Film-Forming Electrolyte Additives on Lithium Metal Batteries via Solid-State NMR/MRI Analysis, *J. Phys. Chem. C.* 125 (2021) 252–265. <https://doi.org/10.1021/acs.jpcc.0c09771>.
- [34] L.E. Marbella, S. Zekoll, J. Kasemchainan, S.P. Emge, P.G. Bruce, C.P. Grey,  $^7\text{Li}$  NMR Chemical Shift Imaging To Detect Microstructural Growth of Lithium in All-Solid-State Batteries, *Chem Mater.* 31 (2019) 2762–2769. <https://doi.org/10.1021/acs.chemmater.8b04875>.
- \*[35] G.J. Rees, D. Spencer Jolly, Z. Ning, T.J. Marrow, G.E. Pavlovskaya, P.G. Bruce, Imaging Sodium Dendrite Growth in All-Solid-State Sodium Batteries Using  $^{23}\text{Na}$  T2-Weighted Magnetic Resonance Imaging, *Angewandte Chemie International Edition.* 60 (2021) 2110–2115. <https://doi.org/10.1002/anie.202013066>. *In situ*  $^{23}\text{Na}$  MRI measurements on an all-solid-state Na//Na battery. Additional contrast is obtained for the deposited Na microstructures using relaxation properties rather than Na concentration.
- [36] J.M. Bray, C.L. Doswell, G.E. Pavlovskaya, L. Chen, B. Kishore, H. Au, H. Alptekin, E. Kendrick, M.-M. Titirici, T. Meersmann, M.M. Britton, Operando visualisation of battery chemistry in a sodium-ion battery by  $^{23}\text{Na}$  magnetic resonance imaging, *Nature Communications.* 11 (2020) 2083. <https://doi.org/10.1038/s41467-020-15938-x>.
- [37] A.I. Freytag, A.D. Pauric, S.A. Krachkovskiy, G.R. Goward, In Situ Magic-Angle Spinning  $^7\text{Li}$  NMR Analysis of a Full Electrochemical Lithium-Ion Battery Using a Jelly Roll Cell Design, *J. Am. Chem. Soc.* 141 (2019) 13758–13761. <https://doi.org/10.1021/jacs.9b06885>.
- [38] V. Küpers, M. Kolek, P. Bieker, M. Winter, G. Brunklaus, In situ  $^7\text{Li}$ -NMR analysis of lithium metal surface deposits with varying electrolyte compositions and concentrations, *Physical Chemistry Chemical Physics.* 21 (2019) 26084–26094. <https://doi.org/10.1039/C9CP05334D>.
- \*[39] Y.-C. Hsieh, M. Leißing, S. Nowak, B.-J. Hwang, M. Winter, G. Brunklaus, Quantification of Dead Lithium via In Situ Nuclear Magnetic Resonance Spectroscopy, *Cell Reports Physical Science.* 1 (2020) 100139. <https://doi.org/10.1016/j.xcrp.2020.100139>. Careful determination and validation of a method to determine by *in situ* and *ex situ* NMR the amount of dead Li and Li trapped in the SEI.

- [40] A.B. Gunnarsdóttir, C.V. Amanchukwu, S. Menkin, C.P. Grey, Noninvasive In Situ NMR Study of “Dead Lithium” Formation and Lithium Corrosion in Full-Cell Lithium Metal Batteries, *J. Am. Chem. Soc.* 142 (2020) 20814–20827. <https://doi.org/10.1021/jacs.0c10258>.
- [41] Y. Xiang, M. Tao, G. Zhong, Z. Liang, G. Zheng, X. Huang, X. Liu, Y. Jin, N. Xu, M. Armand, J.-G. Zhang, K. Xu, R. Fu, Y. Yang, Quantitatively analyzing the failure processes of rechargeable Li metal batteries, *Sci Adv.* 7 (2021) eabj3423. <https://doi.org/10.1126/sciadv.abj3423>.
- [42] C. Wang, M. Liu, M. Thijs, F.G.B. Ooms, S. Ganapathy, M. Wagemaker, High dielectric barium titanate porous scaffold for efficient Li metal cycling in anode-free cells, *Nat Commun.* 12 (2021) 6536. <https://doi.org/10.1038/s41467-021-26859-8>.
- [43] S.A. Krachkovskiy, M. Reza, A.R. Aguilera, I.C. Halalay, B.J. Balcom, G.R. Goward, Real-Time Quantitative Detection of Lithium Plating by In Situ NMR Using a Parallel-Plate Resonator, *J. Electrochem. Soc.* 167 (2020) 130514. <https://doi.org/10.1149/1945-7111/abb7ea>.
- [44] K.J. Sanders, A.R. Aguilera, J.R. Keffer, B.J. Balcom, I.C. Halalay, G.R. Goward, Transient lithium metal plating on graphite: Operando  $^7\text{Li}$  nuclear magnetic resonance investigation of a battery cell using a novel RF probe, *Carbon.* 189 (2022) 377–385. <https://doi.org/10.1016/j.carbon.2021.12.082>.
- \*[45] K. Märker, C. Xu, C.P. Grey, Operando NMR of NMC811/Graphite Lithium-Ion Batteries: Structure, Dynamics, and Lithium Metal Deposition, *J. Am. Chem. Soc.* 142 (2020) 17447–17456. <https://doi.org/10.1021/jacs.0c06727>. Typical *in situ*  $^7\text{Li}$  NMR study of metallic Li deposition onto graphite. The positive NMC electrode  $^7\text{Li}$  signal was measurable and lithium mobility could be measured *in situ* at various temperatures.
- [46] L. Afonso de Araujo, E. Salager, V. Sarou-Kanian, D. Sicsic, M. Deschamps, Operando Nuclear Magnetic Resonance spectroscopy on an NMC622/Graphite battery at low temperature: experimental development and lithium deposition detection, (submitted).
- [47] K. Gotoh, T. Yamakami, I. Nishimura, H. Kometani, H. Ando, K. Hashi, T. Shimizu, H. Ishida, Mechanisms for overcharging of carbon electrodes in lithium-ion/sodium-ion batteries analysed by operando solid-state NMR, *J. Mater. Chem. A.* 8 (2020) 14472–14481. <https://doi.org/10.1039/D0TA04005C>.
- \*[48] J.M. Stratford, A.K. Kleppe, D.S. Keeble, P.A. Chater, S.S. Meysami, C.J. Wright, J. Barker, M.-M. Titirici, P.K. Allan, C.P. Grey, Correlating Local Structure and Sodium Storage in Hard Carbon Anodes: Insights from Pair Distribution Function Analysis and Solid-State NMR, *J. Am. Chem. Soc.* 143 (2021) 14274–14286. <https://doi.org/10.1021/jacs.1c06058>. A careful study of the parameters that influence the  $^{23}\text{Na}$  Knight shift. Na cluster size and degree of order in hard carbon are shown to be of importance.
- [49] E.W. Zhao, T. Liu, E. Jónsson, J. Lee, I. Temprano, R.B. Jethwa, A. Wang, H. Smith, J. Carretero-González, Q. Song, C.P. Grey, In situ NMR metrology reveals reaction mechanisms in redox flow batteries, *Nature.* 579 (2020) 224–228. <https://doi.org/10.1038/s41586-020-2081-7>.
- [50] E.W. Zhao, E. Jónsson, R.B. Jethwa, D. Hey, D. Lyu, A. Brookfield, P.A.A. Klusener, D. Collison, C.P. Grey, Coupled In Situ NMR and EPR Studies Reveal the Electron Transfer Rate and Electrolyte Decomposition in Redox Flow Batteries, *J. Am. Chem. Soc.* 143 (2021) 1885–1895. <https://doi.org/10.1021/jacs.0c10650>.
- [51] S. Wiemers-Meyer, M. Winter, S. Nowak, Chapter Three - NMR as a powerful tool to study lithium ion battery electrolytes, in: G.A. Webb (Ed.), *Annual Reports on NMR Spectroscopy*, Academic Press, 2019: pp. 121–162. <https://doi.org/10.1016/bs.arnmr.2018.12.003>.
- [52] T.-X. Métro, C. Gervais, A. Martinez, C. Bonhomme, D. Laurencin, Unleashing the Potential of  $^{17}\text{O}$  NMR Spectroscopy Using Mechanochemistry, *Angewandte Chemie International Edition.* 56 (2017) 6803–6807. <https://doi.org/10.1002/anie.201702251>.

- [53] F. Geng, M. Shen, B. Hu, Y. Liu, L. Zeng, B. Hu, Monitoring the evolution of local oxygen environments during LiCoO<sub>2</sub> charging via ex situ <sup>17</sup>O NMR, *Chem. Commun.* 55 (2019) 7550–7553. <https://doi.org/10.1039/C9CC03304A>.
- [54] A. Svirinovsky-Arbeli, D. Rosenberg, D. Krotkov, R. Damari, K. Kundu, A. Feintuch, L. Houben, S. Fleischer, M. Leskes, The effects of sample conductivity on the efficacy of dynamic nuclear polarization for sensitivity enhancement in solid state NMR spectroscopy, *Solid State Nuclear Magnetic Resonance*. 99 (2019) 7–14. <https://doi.org/10.1016/j.ssnmr.2019.02.003>.
- [55] T.R. Carver, C.P. Slichter, Polarization of Nuclear Spins in Metals, *Phys. Rev.* 92 (1953) 212–213. <https://doi.org/10.1103/PhysRev.92.212.2>.
- [56] A.J. Ilott, M. Mohammadi, H.J. Chang, C.P. Grey, A. Jerschow, Real-time 3D imaging of microstructure growth in battery cells using indirect MRI, *Proceedings of the National Academy of Sciences*. 113 (2016) 10779–10784. <https://doi.org/10.1073/pnas.1607903113>.